Remote Sensing of Vegetation 10

Approximately 70 percent of the Earth's land surface is covered with vegetation. Furthermore, vegetation is one of the most important components of ecosystems. Knowledge about variations in vegetation species and community distribution patterns, alterations in vegetation phenological (growth) cycles, and modifications in the plant physiology and morphology provide valuable insight into the climatic, edaphic, geologic, and physiographic characteristics of an area (Jones et al., 1998). Scientists have devoted a significant amount of effort to develop sensors and visual and digital image processing algorithms to extract important vegetation biophysical information from remotely sensed data (e.g., Frohn, 1998; Huete and Justice, 1999). Many of the remote sensing techniques are generic in nature and may be applied to a variety of vegetated landscapes, including (Danson, 1998; Lyon et al., 1998):

- agriculture,

- forests,

- rangeland,

- wetland, and

- manicured urban vegetation.

This chapter introduces the fundamental concepts associated with vegetation biophysical characteristics and how remotely sensed data can be processed to provide unique information about these parameters. It then summarizes some of the vegetation indices developed to extract biophysical vegetation information from digital remote sensor data. Several of the metrics used by landscape ecologists to extract meaningful parameters about vegetation patch shape, size, etc., using remote sensor data are then summarized. Case studies are provided throughout the chapter on remote sensing of agriculture, inland wetland, coastal wetland, and biodiversity.

Photosynthesis Fundamentals

Oil and coal today provide more than 90 percent of the energy needed to power automobiles, trains, trucks, ships, airplanes, factories, and a myriad of electrically energized appliances, computers, and communication systems. The energy within oil and coal was originally "captured" from the Sun by plants growing millions of years ago that were transformed into fossil fuels

by geological forces. Therefore, photosynthesis, at least indirectly, is not only the principal means of enabling a civilized society to function normally but also the sole means of sustaining life — except for a few bacteria that derive their energy from sulfur salts and other inorganic compounds. This unique photosynthetic manufacturing process of green plants furnishes raw material, energy, and oxygen. In photosynthesis, energy from the Sun is harnessed and packed into simple sugar molecules made from water and carbon dioxide (CO_2) with the aid of chlorophyll. Oxygen (O_2) is given off as a by-product of the process.

The naturalist Joseph Priestly discovered in 1772 that when he placed a candle in an inverted jar it would burn out quickly, long before it ran out of wax. He also found that a mouse would die if placed under the same jar. He believed that the air was *injured* by the candle and the mouse but that it could be restored by placing a plant under the jar. Jan Ingen-Housz built on Priestly's experiments and discovered in 1788 that the influence of sunlight on the plant could cause it to rescue the mouse in a few hours. In 1796 the French pastor Jean Senebier discovered that it was the carbon dioxide, CO_2, in the jar that was the injured air and that it was actually taken up by the plants. Finally, Theodore de Saussure demonstrated that the increase in the mass of the plant as it grows was due not only to the uptake of CO_2 but also to the uptake of water, H_2O. In the early twentieth century, scientists found that the oxygen for photosynthesis was derived from the water. In effect, light energy entering the plant splits the water into oxygen and hydrogen. The photosynthetic process is described by the equation:

$$6CO_2 + 6H_2O + \text{light energy} \rightarrow C_6H_{12}O_6 + 6O_2 \quad (10\text{-}1)$$
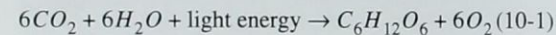
Photosynthesis is an energy-storing process that takes place in leaves and other green parts of plants in the presence of light. The light energy is stored in a simple sugar molecule (glucose) that is produced from carbon dioxide (CO_2) present in the air and water (H_2O) absorbed by the plant primarily through the root system. When the carbon dioxide and the water are combined and form a sugar molecule ($C_6H_{12}O_6$) in a chloroplast, oxygen gas (O_2) is released as a by-product. The oxygen diffuses out into the atmosphere. The photosynthetic process begins when sunlight strikes *chloroplasts*, small bodies in the leaf that contain a green substance called chlorophyll.

Plants have adapted their internal and external structure to perform photosynthesis. This structure and its interaction with electromagnetic energy has a direct impact on how leaves and canopies appear spectrally when recorded using remote sensing instruments.

Spectral Characteristics of Vegetation

A healthy green leaf intercepts incident radiant flux (Φ_i) directly from the Sun or from diffuse skylight scattered onto the leaf. This incident electromagnetic energy interacts with the pigments, water, and intercellular air spaces within the plant leaf. The amount of radiant flux reflected from the leaf (Φ_r), the amount of radiant flux absorbed by the leaf (Φ_α), and the amount of radiant flux transmitted through the leaf (Φ_τ) can be carefully measured as we apply the energy balance equation and attempt to keep track of what happens to all the incident energy. The general equation for the interaction of *spectral* (λ) radiant flux on and within the leaf is

$$\Phi_{i_\lambda} = \Phi_{r_\lambda} + \Phi_{\alpha_\lambda} + \Phi_{\tau_\lambda}. \quad (10\text{-}2)$$

Dividing each of the variables by the original incident radiant flux, Φ_{i_λ}:

$$\frac{\Phi_{i_\lambda}}{\Phi_{i_\lambda}} = \frac{\Phi_{r_\lambda}}{\Phi_{i_\lambda}} + \frac{\Phi_{\alpha_\lambda}}{\Phi_{i_\lambda}} + \frac{\Phi_{\tau_\lambda}}{\Phi_{i_\lambda}} \quad (10\text{-}3)$$

yields

$$i_\lambda = r_\lambda + \alpha_\lambda + \tau_\lambda \quad (10\text{-}4)$$

where r_λ is spectral hemispherical reflectance of the leaf, α_λ is spectral hemispherical absorptance, and τ_λ is spectral hemispherical transmittance by the leaf. Most remote sensing systems function in the 0.35 – 3.0 μm region measuring primarily reflected energy. Therefore, it is useful to think of this relationship as:

$$r_\lambda = i_\lambda - (\alpha_\lambda + \tau_\lambda) \quad (10\text{-}5)$$

where the energy reflected from the plant leaf surface is equal to the incident energy minus the energy absorbed directly by the plant for photosynthetic or other purposes and the amount of energy transmitted directly through the leaf onto other leaves or the ground beneath the canopy.

Dominant Factors Controlling Leaf Reflectance

Pioneering work by Gates et al. (1965), Gausmann et al. (1969), Myers (1970) and others demonstrated the importance of understanding how leaf pigments, internal scattering, and leaf water content affect the reflectance and transmittance properties of leaves (Peterson and Running,
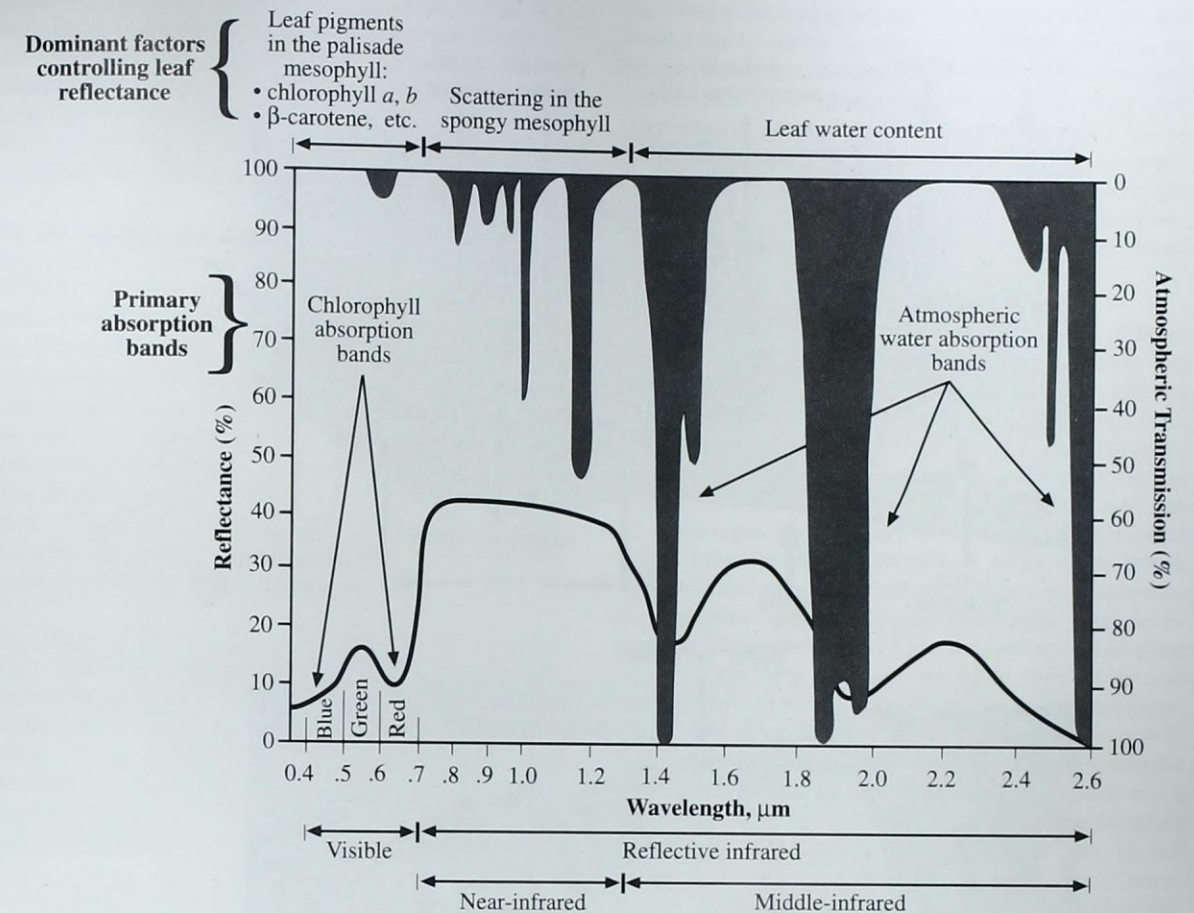

Figure 10-1 Spectral reflectance characteristics of healthy, green vegetation for the wavelength interval 0.4 – 2.6 μm. The dominant factors controlling leaf reflectance are the various leaf pigments in the palisade mesophyll (e.g., chlorophyll *a* and *b*, and β-carotene), the scattering of near-infrared energy in the spongy mesophyll, and the amount of water in the plant. The primary chlorophyll absorption bands occur at 0.43 – 0.45 μm and 0.65 – 0.66 μm in the visible region. The primary water absorption bands occur at 0.97, 1.19, 1.45, 1.94, and 2.7 μm.

1989). Dominant factors controlling leaf reflectance in the region from 0.35 – 2.6 μm are summarized in Figure 10-1.

Visible Light Interaction with Pigments in the Palisade Mesophyll Cells

The process of food-making via photosynthesis determines how a leaf and the associated plant canopy actually appear radiometrically on remotely sensed images. A healthy leaf needs three things to make food:

- carbon dioxide (CO_2),

- water (H_2O), and

- irradiance (E_λ) measured in W m^{-2}.

The carbon dioxide from the air and the water provided by the root and stem system represent the fundamental raw materials of photosynthesis. Sunlight provides the irradiance (E_λ) that powers photosynthesis.

The leaf is the primary photosynthesizing organ. A cross-section of a typical green leaf is shown in Figure 10-2. The cell structure of leaves is highly variable depending upon species and environmental conditions during growth. Carbon dioxide enters the leaf from the atmosphere through tiny pores called *stomata* or *stoma,* located primarily on the underside of the leaf on the *lower epidermis*. Each stomata is
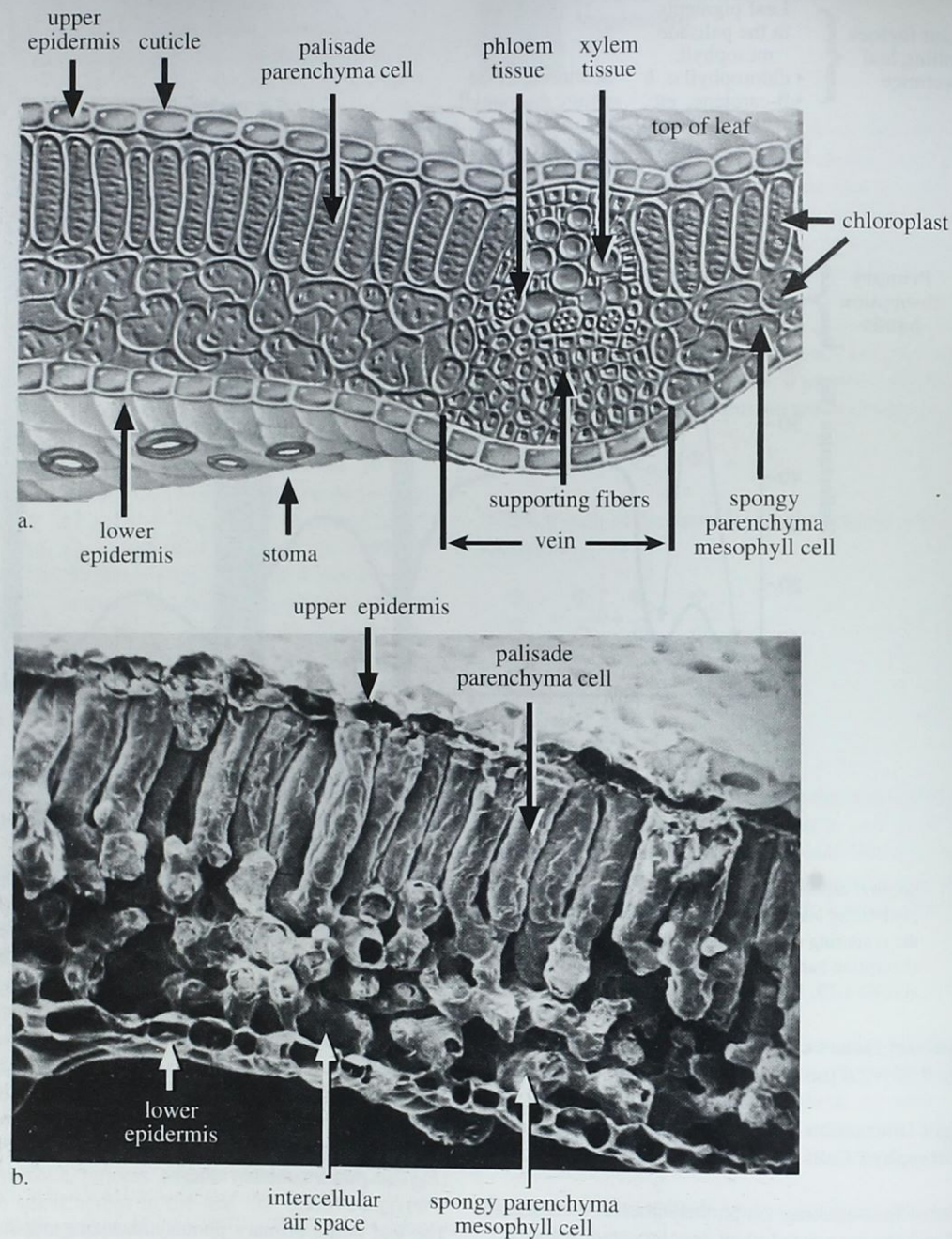
a.

b.

Figure 10-2   a) Hypothetical cross-section of a typical healthy green leaf, showing both the top and underside of the leaf. The chlorophyll pigments in the palisade parenchyma cells have a significant impact on the absorption and reflectance of visible light (blue, green, and red), while the spongy parenchyma mesophyll cells have a significant impact on the absorption and reflectance of near-infrared incident energy. b) Electron microscope image of a green leaf.

surrounded by *guard cells* that swell or contract. When they swell, the stomata pore opens and allows carbon dioxide to enter the leaf. A typical sunflower leaf might have 2 million stomata, but they make up only about 1 percent of the leaf's surface area. Usually, there are more stomata on the bottom of a leaf; however, on some leaves the stomata are evenly distributed on both the upper and lower epidermis.

The top layer of leaf *upper epidermis* cells has a *cuticular* surface that diffuses but reflects very little light (Philpott, 1971). It is variable in thickness but is often only 3 – 5 μm thick with cell dimensions of approximately 18 x 15 x 20 μm. It is useful to think of it as a waxy, translucent material similar to the cuticle at the top of your fingernail. Leaves of many plants that grow in bright sunlight have a thick cuticle that can filter out some light and guard against excessive plant water loss. Conversely, some plants such as ferns and some shrubs on the forest floor must survive in shaded conditions. The leaves of many of these plants have a thin cuticle so that the plant can collect as much of the dim sunlight as possible for photosynthesis.

Many leaves in direct sunlight have hairs growing out of the upper (and lower) epidermis, causing them to feel fuzzy. These hairs can be beneficial, as they reduce the intensity of the incident sunlight to the plant. Nevertheless, much of the visible and near-infrared wavelength energy is transmitted through the cuticle and upper epidermis to the palisade parenchyma mesophyll cells and spongy parenchyma mesophyll cells below.

Photosynthesis occurs inside the typical green leaf in two kinds of food-making cells — *palisade parenchyma* and *spongy parenchyma* mesophyll cells. Most leaves have a distinct layer of long palisade parenchyma cells in the upper part of the mesophyll and more irregularly shaped, loosely arranged spongy parenchyma cells in the lower part of the mesophyll. The palisade cells tend to form in the portion of the mesophyll toward the side from which the light enters the leaf. In most horizontal (planophile) leaves the palisade cells will be toward the upper surface, but in leaves that grow nearly vertical (erectophile), the palisade cells may form from both sides. In some leaves the elongated palisade cells are entirely absent and only spongy parenchyma cells will exist within the mesophyll.

The cellular structure of the leaf is large compared to the wavelengths of light that interact with it. Palisade cells are typically 15 x 15 x 60 μm, while spongy mesophyll parenchyma cells are smaller. The palisade parenchyma mesophyll plant cells contain chloroplasts with chlorophyll pigments.

The chloroplasts are generally 5 – 8 μm in diameter and about 1 μm in width. As many as 50 chloroplasts may be present in each parenchyma cell. Within the chloroplasts are long slender *grana* strands (not shown) within which the chlorophyll is actually located (approximately 0.5 μm in length and 0.05 μm in diameter). The chloroplasts are generally more abundant toward the upper side of the leaf in the palisade cells and hence account for the darker green appearance of the upper leaf surface compared with the bottom lighter surface.

A molecule, when struck by a wave or photon of light, reflects some of the energy or it can absorb the energy and thus enter into a higher energy or excited state (refer to Chapter 2). Each molecule absorbs or reflects its own characteristic wavelengths of light. Molecules in a typical green plant have evolved to absorb wavelengths of light in the visible region of the spectrum (0.35 – 0.70 μm) very well and are called *pigments*. An *absorption spectrum* for a particular pigment describes the wavelengths at which it can absorb light and enter into an excited state. Figure 10-3a presents the absorption spectrum of pure chlorophyll pigments in solution. Chlorophyll *a* and *b* are the most important plant pigments absorbing blue and red light: chlorophyll *a* at wavelengths of 0.43 and 0.66 μm and chlorophyll *b* at wavelengths of 0.45 and 0.65 μm (Curran, 1983; Farabee, 1997). A relative lack of absorption in the wavelengths between the two chlorophyll absorption bands produces a trough in the absorption efficiency at approximately 0.54 μm in the green portion of the electromagnetic spectrum (Figure 10-3a). Thus, it is the relatively lower absorption of green wavelength light (compared to blue and red light) by the leaf that causes healthy green foliage to appear green to our eyes.

There are other pigments present in the palisade mesophyll cells that are usually masked by the abundance of chlorophyll pigments. For example, there are yellow *carotenes* and pale yellow *xanthophyll* pigments, with strong absorption primarily in the blue wavelength region. The β-carotene absorption spectra is shown in Figure 10-3b with its strong absorption band centered at about 0.45 μm. *Phycoerythrin* pigments may also be present in the leaf which absorb predominantly in the green region centered at about 0.55 μm, allowing blue and red light to be reflected. *Phycocyanin* pigments absorb primarily in the green and red regions centered at about 0.62 μm, allowing much of the blue and some of the green light (i.e., the combination produces cyan) to be reflected (Figure 10-3b). Because chlorophyll *a* and *b* chloroplasts are also present and have a similar absorption band in this blue region, they tend to dominate and mask the effect of the other pigments present. When a plant undergoes senescence in the fall or encounters stress, the chlorophyll
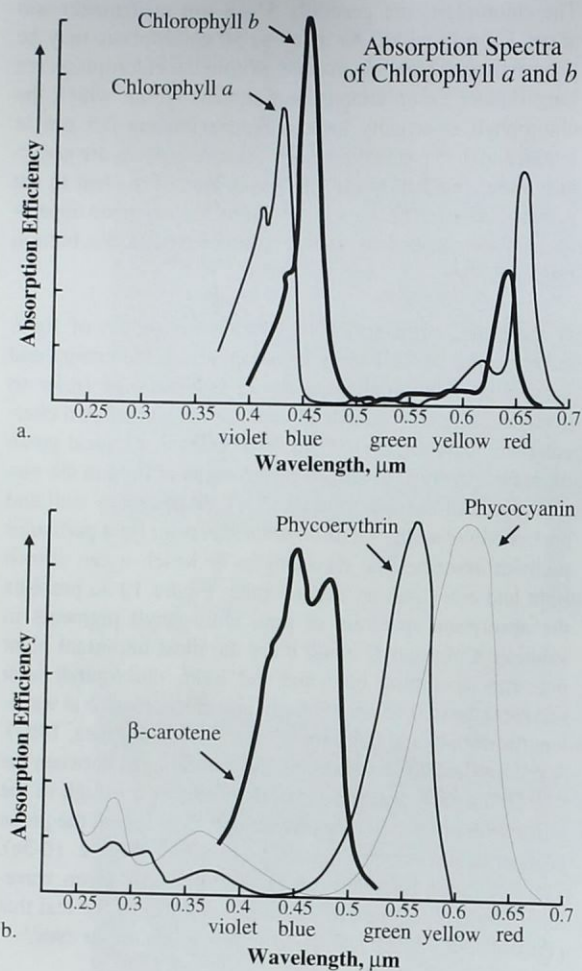
Figure 10-3   a) Absorption spectra of chlorophyll a and b pigments. Chlorophyll a and b pigments in a leaf absorb much of the incident blue and red wavelength energy. b) Absorption spectra of β-carotene, which absorbs primarily in the blue. Other pigments that might be found in a leaf include Phycoerythrin which absorbs primarily green light, and Phycocyanin which absorbs primarily green and red light (after Farabee, 1997).

pigment may disappear, allowing the carotenes and other pigments to become dominant. For example, in the fall, chlorophyll production ceases, causing the yellow coloration of the carotenes and other specific pigments in the tree foliage to become more visible to our eyes. In addition, some trees produce great quantities of *anthocyanin* in the fall, causing the leaves to appear bright red.

The two optimum spectral regions for sensing the chlorophyll absorption characteristics of a leaf are believed to be 0.45 – 0.52 μm and 0.63 – 0.69 μm (Figure 10-3a). The former region is characterized by strong absorption by carotenoids and chlorophylls, whereas the latter is characterized by strong chlorophyll absorption. Remote sensing of chlorophyll absorption within a canopy represents a fundamental biophysical variable useful for many biogeographical investigations. The absorption characteristics of plant canopies may be coupled with other remotely sensed data to identify vegetation stress, yield, and other hybrid variables. Thus, many remote sensing studies are concerned with monitoring what happens to the *photosynthetically active radiation* (PAR) as it interacts with individual leaves and/or the plant canopy. The use of high spectral resolution imaging spectrometers are particularly useful for measuring the absorption and reflectance characteristics of the photosynthetically active radiation.

To demonstrate these principles, consider the spectral reflectance characteristics of four different leaves obtained from a single healthy Sweetgum tree (*Liquidambar styraciflua* L.) on November 11, 1998, in Columbia, SC (Color Plate 10-1). The green leaf (a), yellow leaf (b), and red leaf (c) were still on the Sweetgum tree at the time of data collection. The dark brown leaf (d) was collected on the ground beneath the tree.

A GER 1500 (Geophysical & Environmental Research, Inc.) handheld spectroradiometer was used to obtain spectral reflectance measurements from each of the leaves. The spectroradiometer obtained spectral reflectance measurements in 512 bands in the ultraviolet, blue, green, red, and near-infrared spectral regions from 350 – 1050 nm. Percent reflectance measurements were obtained in the laboratory by measuring the amount of energy reflected from the surface of the leaf (the target) divided by the amount of energy reflected from a Spectralon® reflectance reference (percent reflectance = target/reference * 100). The reflectance measurements for each of the leaves from 400 – 1050 nm were plotted in a percent reflectance graph (Color Plate 10-1e).

The green leaf (Color Plate 10-1a) was still photosynthesizing and yielded a typical healthy green reflectance spectra with strong chlorophyll absorption bands in the blue and red regions (approximately 6 percent reflectance at 450 nm and 5 percent at 650 nm, respectively), and a peak in reflectance in the green region of the visible spectrum (11 percent at 550 nm). Approximately 76 percent of the incident near-infrared radiant flux was reflected from the leaf at 900 nm.

The yellow leaf (Color Plate 10-1b) was undergoing senescence. As the influence of the chlorophyll pigments dimin-

ished, relatively greater amounts of green (24 percent at 550 nm) and red (32 percent at 650 nm) light were reflected from the leaf, resulting in a yellow appearance. At 750 nm the yellow leaf reflected less near-infrared radiant flux than the healthy green leaf. However, near-infrared reflectance at 900 nm was about 76 percent, very similar to the healthy green leaf.

The red leaf (Color Plate 10-1c) reflected 7 percent of the blue at 450 nm, 6 percent of the green energy at 550 nm, and approximately 23 percent of the incident red energy at 650 nm. Near-infrared reflectance at 900 nm dropped to 70 percent.

The dark brown leaf (Color Plate 10-1d) produced a spectral reflectance curve with low blue (7 percent at 450 nm), green (9 percent at 550 nm), and red reflectance (10 percent at 650 nm). This combination produced a dark brown appearance. Near-infrared reflectance dropped to 44 percent at 900 nm.

It is important to understand the physiology of the plants under investigation and especially their pigmentation characteristics so that we can appreciate how a typical plant will appear when chlorophyll absorption starts to decrease, either due to seasonal senescence or environmental stress. As demonstrated, when a plant is under stress and/or chlorophyll production decreases, the lack of chlorophyll pigmentation typically causes the plant to absorb less in the chlorophyll absorption bands. Such plants will have a much higher reflectance, particularly in the green and red portion of the spectrum, and therefore may appear yellowish or *chlorotic*. In fact, Carter (1993) suggests that increased reflectance in the visible spectrum is the most consistent leaf reflectance response to plant stress. Infrared reflectance responds consistently only when stress has developed sufficiently to cause severe leaf dehydration (to be demonstrated shortly).

Leaf spectral reflectance is most likely to indicate plant stress first in the sensitive 535 – 640 and 685 – 700 nm visible light wavelength ranges. Increased reflectance near 700 nm represents the often reported "blue shift of the red edge," i.e., the shift toward shorter wavelengths of the red-infrared transition curve that occurs in stressed plants when reflectance is plotted versus wavelength (Cibula and Carter, 1992). The shift toward shorter wavelengths in the region from 650 – 700 nm is particularly evident for the yellow and red reflectance curves shown in Color Plate 10-1e. Remote sensing within these spectrally narrow ranges may provide improved capability to detect plant stress not only in individual leaves but for whole plants and perhaps for densely vegetated canopies (Carter, 1993; Carter et al., 1996).

Normal color film is sensitive to blue, green, and red wavelength energy. Color-infrared film is sensitive to green, red, and near-infrared energy after minus-blue (yellow) filtration (Rundquist and Sampson, 1988; refer to Chapter 4). Therefore, even the most simple camera with color or color-infrared film and appropriate band-pass filtration (i.e., only certain wavelengths of light are allowed to pass) can be used to remotely sense differences in spectral reflectance caused by the pigments present in the palisade parenchyma layer of cells in a typical leaf. However, to detect very subtle spectral reflectance differences in the relatively narrow bands suggested by Cibula and Carter (1992) and Carter et al. (1996), it may be necessary to use a high spectral resolution imaging spectroradiometer that has very narrow bandwidths.

Near-Infrared Energy Interaction Within the Spongy Mesophyll Cells

In a typical healthy green leaf, the near-infrared reflectance increases dramatically in the region from 700 - 1200 nm. For example, the healthy green leaf in the previous example reflected approximately 76 percent of the incident near-infrared energy at 900 nm. Healthy green leaves absorb radiant energy very efficiently in the blue and red portions of the spectrum where incident light is required for photosynthesis. But immediately to the long wavelength side of the red chlorophyll absorption band, why does the reflectance and transmittance of plant leaves increase so dramatically, causing the absorptance to fall to low values (Figure 10-1)? This condition occurs throughout the near-infrared wavelength range where the direct sunlight incident on plants has the bulk of its energy. If plants absorbed this energy with the same efficiency as they do in the visible region, they could become much too warm and the proteins would be irreversibly denatured. As a result, plants have adapted so they do not use this massive amount of near-infrared energy and simply reflect it or transmit it through to underlying leaves or the ground.

The spongy mesophyll layer in a green leaf controls the amount of near-infrared energy that is reflected. The spongy mesophyll layer typically lies below the palisade mesophyll layer and is composed of many cells and intercellular air spaces as shown in Figure 10-2. It is here that the oxygen and carbon dioxide exchange takes place for photosynthesis and respiration. In the near-infrared region, healthy green vegetation is generally characterized by high reflectance (40 – 60 percent), high transmittance (40 – 60 percent) through the leaf onto underlying leaves, and relatively low absorptance (5 – 10 percent). Notice that a healthy green leaf's reflectance and transmittance spectra throughout the visible and near-infrared portion of the spectrum are almost mirror
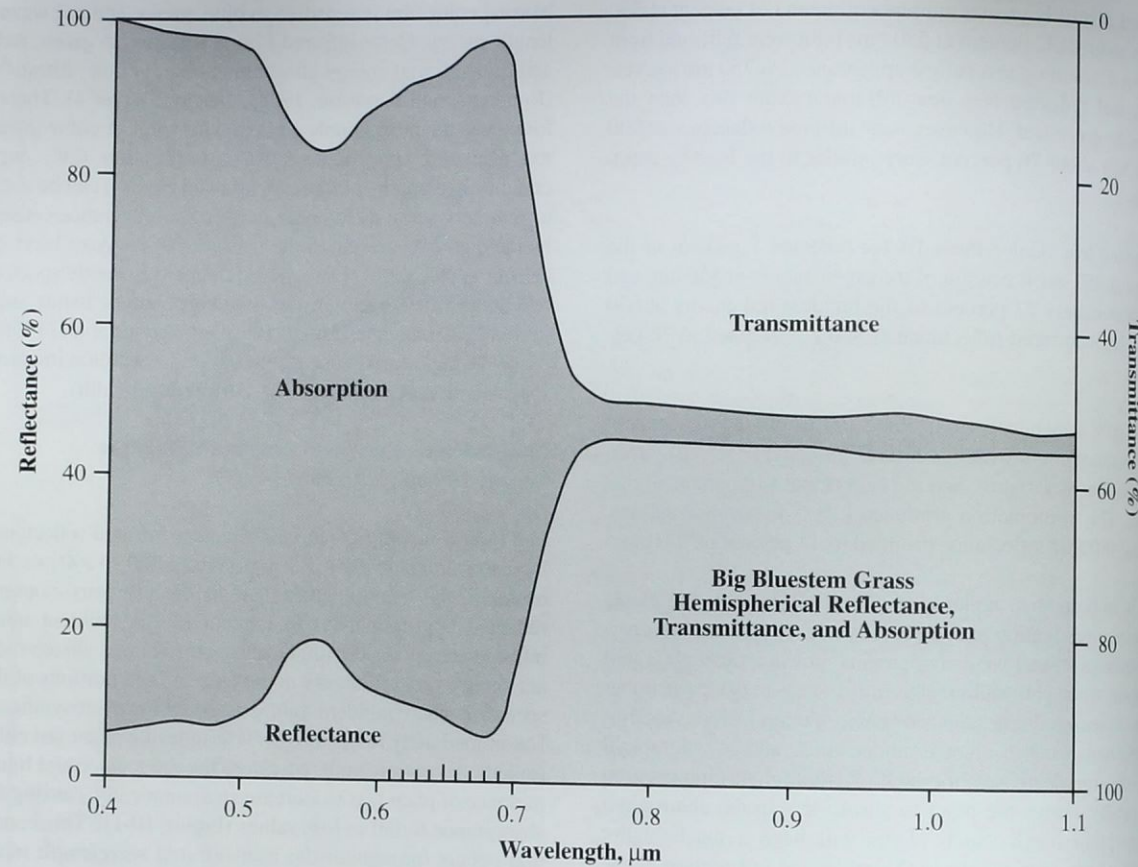
Figure 10-4　Hemispherical reflectance, transmittance, and absorption characteristics of Big Bluestem grass adaxial leaf surfaces obtained using a laboratory spectroradiometer. The reflectance and transmittance curves are almost mirror images of one another throughout the visible and near-infrared portions of the electromagnetic spectrum. The blue and red chlorophyll in plants absorb much of the incident energy in the visible portion of the spectrum (0.4 – 0.7 μm) (after Walter-Shea and Biehl, 1990). Imaging spectrometers such as AVIRIS are capable of identifying small changes in the absorption and reflection characteristics of plants because the sensors often have channels that are only 10 nm apart, i.e., we could have 10 channels in the region from 0.6 – 0.7 μm (600 to 700 nm).

Figure 10-5　A hypothetical example of additive reflectance from a canopy with two leaf layers. Fifty percent of the incident radiant flux, Φ_i, to leaf 1 is reflected (R_1) and the other 50 percent is transmitted onto leaf 2 (T_1). Fifty percent of the radiant flux incident to leaf 2 is transmitted through leaf 2 (T_2), the other 50 percent is reflected toward the base of leaf 1 (R_2). Fifty percent of the energy incident at the base of leaf 1 is transmitted through it (T_3) while the remaining 50 percent (R_3) is reflected toward leaf 2 once again. At this point, an additional 12.5 percent (1/8) reflectance has been contributed by leaf 2, bringing the total reflected radiant flux to 62.5 percent. However, to be even more accurate, one would have to also take into account the amount of energy reflected from the base of leaf 1 (R_3) onto leaf 2, the amount reflected from leaf 2 (R_4), and eventually transmitted through leaf 1 once again (T_5). This process would continue.

images of one another, as shown in Figure 10-4 (Walter-Shea and Biehl, 1990).

The high diffuse reflectance of the near-infrared (0.7 – 1.2 μm) energy from plant leaves is due to the internal scattering at the cell wall-air interfaces within the leaf (Gausmann et al., 1969; Peterson and Running, 1989). A water vapor absorption band exists at 0.92 – 0.98 μm; consequently, the optimum spectral region for sensing in the near-infrared region is believed to be 0.74 – 0.90 μm (Tucker, 1978).

The main reasons that healthy plant canopies reflect so much near-infrared energy are:

• the leaf already reflects 40 – 60 percent of the incident near-infrared energy from the spongy mesophyll (Figure 10-4), and

• the remaining 45 – 50 percent of the energy penetrates (i.e., is transmitted) through the leaf and can be reflected once again by leaves below it.

This is called *leaf additive reflectance*. For example, consider the reflectance and transmission characteristics of the hypothetical two-layer plant canopy shown in Figure 10-5. Assume that leaf 1 reflects 50 percent of the incident near-infrared energy back into the atmosphere and that the
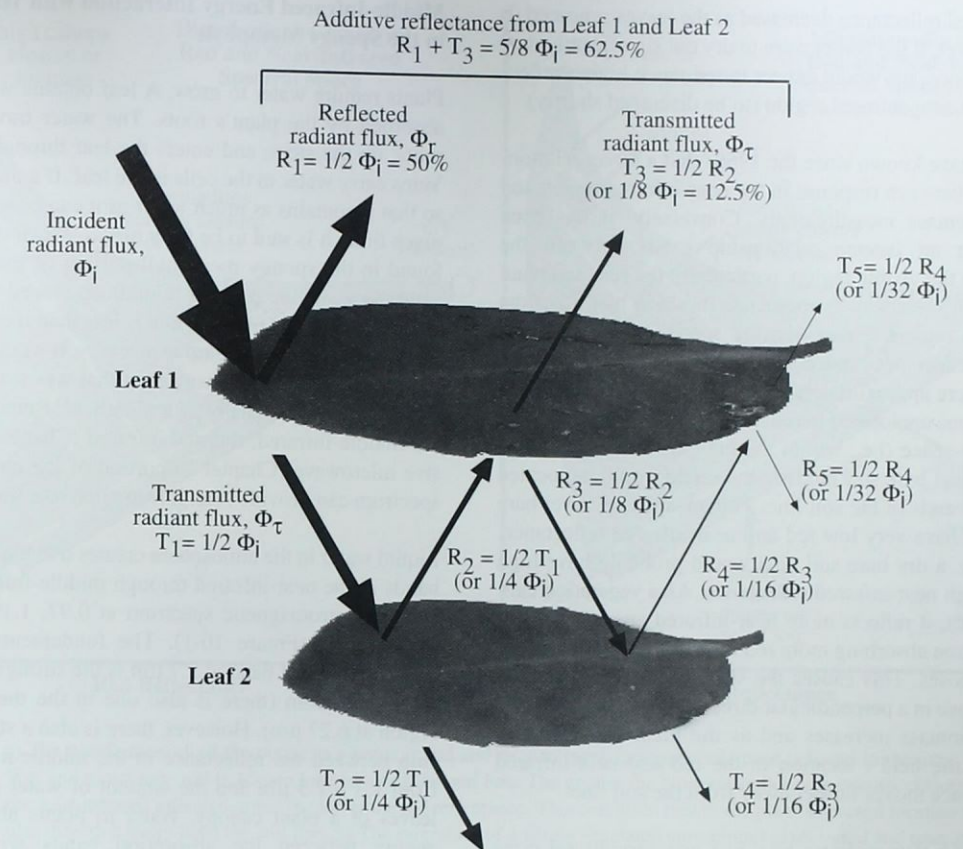
remaining 50 percent of the near-infrared energy is transmitted through leaf 1 onto leaf 2. The transmitted energy then falls on leaf 2 where 50 percent again is transmitted (25 percent of the original) and 50 percent is reflected. The reflected energy then passes back through leaf 1 which allows half of that energy (or 12.5 percent of the original) to be transmitted and half reflected. The resulting total energy exiting leaf 1 in this two-layer example is 62.5 percent of the incident energy. Therefore, the greater the number of leaf layers in a healthy, mature canopy, theoretically the greater the infrared reflectance. Conversely, if the canopy is only composed of a single, sparse leaf layer then the near-infrared reflectance will

not be as great because the energy that is transmitted through the leaf layer may be absorbed by the ground cover beneath.

It is important to point out that changes in the near-infrared spectral properties of healthy green vegetation may provide information about plant senescence and/or stress. For example, consider the four leaves and their spectral reflectance characteristics shown in Color Plate 10-1. The photosynthesizing green leaf (a) exhibited strong chlorophyll absorption in the blue and red wavelength regions, an understandable increase in green reflectance, and approximately 76 percent reflectance in the near-infrared region. After a certain point,

near-infrared reflectance decreased as the leaves senesced (b – d). However, if the leaves were to dry out significantly during senescence, we would expect to see much higher reflectance in the near-infrared region (to be discussed shortly).

Scientists have known since the 1960s that a *direct* relationship exists between response in the near-infrared region and various biomass measurements. Conversely, it has been shown that an *inverse* relationship exists between response in the visible region, particularly the red, and plant biomass. The best way to appreciate this is to plot all of the pixels in a typical remote sensing scene in red and near-infrared reflectance space. For example, Figure 10-6a depicts where approximately 10,000 pixels in a typical agricultural scene are located in red and near-infrared multispectral feature space (i.e., within the gray area). Dry bare soil fields and wet bare soil fields in the scene would be located at opposite ends of the soil line. This means that a wet bare soil would have very low red and near-infrared reflectance. Conversely, a dry bare soil area would probably have high red and high near-infrared reflectance. As a vegetation canopy matures, it reflects more near-infrared energy while at the same time absorbing more red radiant flux for photosynthetic purposes. This causes the spectral reflectance of the pixel to move in a perpendicular direction away from the soil line. As biomass increases and as the plant canopy cover increases, the field's location in the red and near-infrared spectral space moves farther away from the soil line.

Figure 10-6b demonstrates how just one agricultural pixel might move about in the red and near-infrared spectral space during a typical growing season. If the field was prepared properly, it would probably be located in the moist bare soil region of the soil line with low red and low near-infrared reflectance at the beginning of the growing season. After the crop emerges, it would depart from the soil line, eventually reaching complete canopy closure. At this point the reflected near-infrared radiant flux would be high and the red reflectance would be low. After harvesting, the pixel would probably be found once again on the soil line but perhaps in a drier condition.

The relationship between red and near-infrared canopy reflectance has resulted in the development of numerous remote sensing vegetation indices and biomass-estimating techniques that utilize multiple measurements in the visible and near-infrared region (e.g., Richardson and Everitt, 1992; Lyon et al., 1998). The result is a linear combination that may be more highly correlated with biomass than either red or near-infrared measurement alone. Several of these algorithms are summarized in the section on Vegetation Indices in this chapter.

Middle-Infrared Energy Interaction with Water in the Spongy Mesophyll

Plants require water to grow. A leaf obtains water that was absorbed by the plant's roots. The water travels from the roots, up the stem, and enters the leaf through the *petiole*. Veins carry water to the cells in the leaf. If a plant is watered so that it contains as much water as it can possibly hold at a given time, it is said to be fully *turgid*. Much of the water is found in the spongy mesophyll portion of the plant. If we forget to water the plant or rainfall decreases, the plant will contain an amount of water that is less than it can potentially hold. This is called its *relative turgidity*. It would be useful to have a remote sensing instrument that was sensitive to how much water was actually in a plant leaf. Remote sensing in the middle-infrared, thermal infrared (Chapter 8), and passive microwave (Chapter 9) portion of the electromagnetic spectrum can provide such information to a limited extent.

Liquid water in the atmosphere creates five major absorption bands in the near-infrared through middle-infrared portions of the electromagnetic spectrum at 0.97, 1.19, 1.45, 1.94, and 2.7 μm (Figure 10-1). The fundamental vibrational water-absorption band at 2.7 μm is the strongest in this part of the spectrum (there is also one in the thermal infrared region at 6.27 μm). However, there is also a strong relationship between the reflectance in the middle-infrared region from 1.3 – 2.5 μm and the amount of water present in the leaves of a plant canopy. Water in plants absorb incident energy between the absorption bands with increasing strength at longer wavelengths. In these middle-infrared wavelengths, vegetation reflectance peaks occur at about 1.6 and 2.2 μm, between the major atmospheric water absorption bands (Figure 10-1).

Water is a good absorber of middle-infrared energy, so the greater the turgidity of the leaves, the lower the middle-infrared reflectance. Conversely, as the moisture content of leaves decreases, reflectance in the middle-infrared region increases substantially. As the amount of plant water in the intercellular air spaces decreases, this causes the incident middle-infrared energy to be more intensely scattered at the interface of the intercellular walls resulting in greater middle-infrared reflectance from the leaf. For example, consider the spectral reflectance of Magnolia leaf samples at five different moisture conditions displayed over the wavelength interval from 0.4 – 2.5 μm (Figure 10-7). The middle-infrared wavelength intervals from about 1.5 – 1.8 μm and from 2.1 – 2.3 μm appear to be more sensitive to changes in the moisture content of the plants than the visible or near-infrared portions of the spectrum (i.e., the y-axis distance between the spectral reflectance curves is greater as the
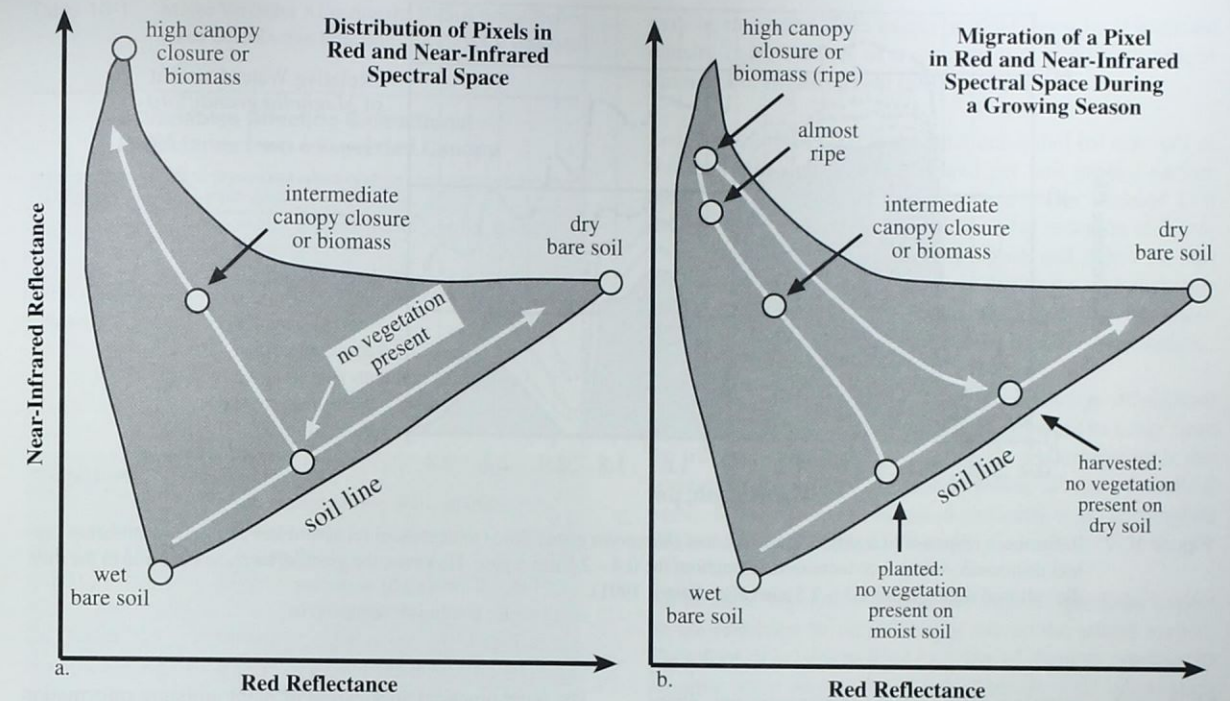

Figure 10-6 a) The distribution of all the pixels in a scene in red and near-infrared multispectral space is found in the gray shaded area. Wet and moist bare soil fields are located along the soil line. The greater the biomass and/or crop canopy closure, the greater the near-infrared reflectance and the lower the red reflectance. This condition moves the pixel's spectral location a perpendicular direction away from the soil line. b) The migration of a single vegetated agricultural pixel in red and near-infrared multispectral space during a growing season is shown. After the crop emerges, it departs from the soil line, eventually reaching complete canopy closure. After harvesting, the pixel will be found on the soil line, but perhaps in a drier soil condition.

moisture content decreases). Also note that substantive changes in the visible reflectance curves (0.4 – 0.7 μm) did not begin to appear until the plant moisture in the leaves decreased to about 50 percent. When the relative water content of the plant decreases to 50 percent, almost any portion of the visible, near- and middle-infrared regions might provide some valuable spectral reflectance information.

Leaf reflectance in the middle-infrared region is inversely related to the absorptance of a layer of water approximately 1 mm in depth (Carter, 1991). The degree to which incident solar energy in the middle-infrared region is absorbed by vegetation is a function of the total amount of water present in the leaf and the leaf thickness. If proper choices of sensors and spectral bands are made, it is possible to monitor the relative turgidity in plants.

Most optical remote sensing systems (except radar) are generally constrained to function in the wavelength intervals from 0.3 – 1.3, 1.5 – 1.8, and 2.0 – 2.6 μm due to the strong atmospheric water absorption bands at 1.45, 1.94, and 2.7 μm. Fortunately, as demonstrated in Figure 10-7, there is a strong "carry over" sensitivity to water content in the 1.5 – 1.8 and 2.0 – 2.6 μm regions adjacent to the major water absorption bands. This is the reason that the Landsat Thematic Mapper (4 and 5) and Landsat 7 Enhanced Thematic Mapper Plus (ETM[+]) were made sensitive to two bands in this region: band 5 (1.55 – 1.75 μm) and band 7 (2.08 – 2.35 μm). The 1.55 – 1.75 μm middle-infrared band has consistently demonstrated a sensitivity to canopy moisture content. For example, Pierce et al. (1990) found that this band and vegetation indices produced using it were correlated with canopy water stress in coniferous forests.
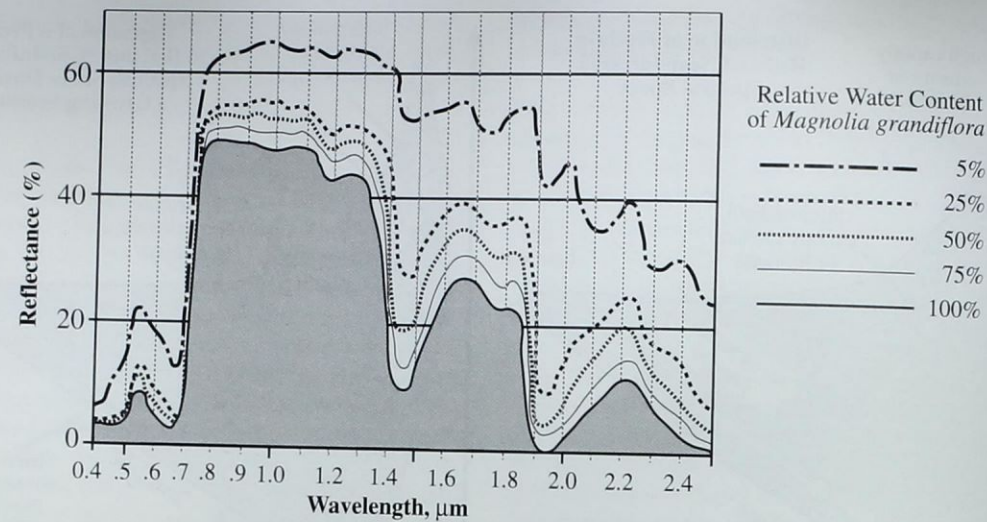
Figure 10-7   Reflectance response of a single Magnolia leaf (*Magnolia grandiflora*) to decreased relative water content. As moisture content decreased, reflectance increased throughout the 0.4 – 2.5 μm region. However, the greatest increase occurred in the middle-infrared region from 1.3 – 2.5 μm (after Carter, 1991).

Much of the water in a plant is lost via transpiration. *Transpiration* occurs as the Sun warms the water inside the leaf, causing some of the water to change its state to water vapor that escapes through the stomata. The following are several important functions that transpiration performs:

- It cools the inside of the leaf because the escaping water vapor contains heat.

- It keeps water flowing up from the roots, through the stem, to the leaves.

- It ensures a steady supply of dissolved minerals from the soil.

As molecules of water vapor at the top of the leaf in the tree are lost to transpiration, the entire column of water is pulled upward. Plants lose a considerable amount of water through transpiration each day. For example, a single corn plant can lose about 4 quarts (3.8 liters) of water on a very hot day. If the roots of the plant cannot replace this water, the leaves wilt, photosynthesis stops, and the plant dies. Thus, monitoring the moisture content of plant canopies, which is correlated with rates of transpiration, can provide valuable information on the health of a crop or stand of vegetation. Thermal infrared and passive microwave remote sensing have provided valuable plant canopy evapotranspiration information.

The most practical application of plant moisture information is the regional assessment of crop water conditions for irrigation scheduling, stress assessment, and yield modeling for agriculture, rangeland, and forestry management.

Advanced Vegetation Spectral Reflectance Characteristics: the Bidirectional Reflectance Distribution Function (BRDF)

It would be wonderful if a vegetated canopy such as a mature corn crop or Loblolly pine plantation reflected the same amount of radiant flux toward the sensor irrespective of 1) the solar incidence and azimuth angles, or 2) the sensor viewing geometry. This would mean that the vegetated canopy was a true Lambertian surface, i.e., it reflects incident energy equally well in all directions. Unfortunately, considerable research has demonstrated that this is not the case (e.g., Kimes, 1983). In fact, the spectral radiant flux leaving a vegetation canopy is significantly impacted by a number of factors, many of which are listed in Table 10-1. We briefly discuss the primary vegetation parameters and then delve more deeply into Sun illumination and sensor system geometric characteristics.

The amount and spectral distribution of radiant flux leaving a vegetated canopy is influenced by the type of vegetation present. For example, grasses hopefully reflect energy differently than a mature stand of trees. Some vegetated canopies

Table 10-1.   Major Variables Affecting the Bidirectional Reflectance Distribution Function (BRDF) of a Vegetated Canopy

Variables Affecting Bidirectional Reflectance from a Vegetated Canopy	

Illumination	• Geometry
	   - angle-of-incidence of Sun (or Radar)
	   - azimuth
	• Spectral characteristics (λ)

Sensor	• Geometry
	   - angle of view (e.g., 0° nadir)
	   - azimuth look direction (0 – 360°)
	• Spectral sensitivity (λ)
	• IFOV (milliradians)

Vegetation	• Canopy
	   - type (plant or tree nominal class)
	   - closure (%)
	   - orientation
	     - systematic (e.g., rows 0 – 360°)
	     - unsystematic (random)
	• Crown
	   - shape (e.g., circular, conical)
	   - diameter (m)
	• Trunk or Stem
	   - density (units per m²)
	   - tree diameter-at-breast-height (DBH)
	• Leaf
	   - leaf-area-index (LAI)
	   - leaf-angle-distribution (LAD) (planophile, erectophile)

Understory	same as vegetation
Soil	• Texture • Color • Moisture content

have 100 percent *canopy closure* meaning that the understory and soil beneath are not visible through the canopy. Conversely, some canopies have < 100 percent canopy closure, allowing portions of the understory and/or soil to reflect energy into the instantaneous field of view (IFOV) of the sensor, creating a hybrid or mixed pixel. It is possible to disentangle the spectral contribution from the individual land covers, but it requires considerable image processing expertise.

Some vegetation is oriented randomly while other vegetation is often systematically arranged in rows in a cardinal direction (0 – 360°). Individual tree crowns often have unique shapes (e.g., a conical Ponderosa pine crown or circular Blackjack oak crown) with unique tree crown diameters that

may be measured. Tree trunks or plant stems have a certain density (e.g., number of trunks per unit area) with unique *diameter-at-breast-height* (DBH) values.

Leaf-area-index (LAI) is the total one-sided (or one half of the total all-sided) green leaf area per unit ground-surface area. It is an important biological parameter because 1) it defines the area that interacts with solar radiation and provides much of the remote sensing signal, and 2) it is the surface that is responsible for carbon absorption and exchange within the atmosphere (Chen and Black, 1992). Some canopies have substantially higher leaf-area-indices than others.

The *leaf-angle-distribution* (LAD) may change throughout the day as the leaves orient themselves toward or away from the incident radiation. Some leaves lie predominantly in the horizontal plane (e.g., planophile leaves in many broadleaf trees), while others are oriented vertically (e.g., erectophile leaves of coastal cordgrass marsh).

All of these vegetation factors can have a significant impact on the reflection of incident light toward the sensor system. Therefore, it is best to hold as many of them as constant as possible when attempting to extract biophysical information such as primary productivity or biomass using multiple dates of remote sensor data. Even if we held these variables as constant as possible, the zenith and azimuth angles of the incident solar radiation and the azimuth and viewing angle of the sensor system can introduce such dramatic effects that we may not be able to compare our spectral reflectance measurements obtained at one time with those of another. Fortunately, if we know a great deal about the vegetation characteristics of the canopy (just discussed) and obtain some information about the bidirectional reflectance characteristics of the solar angle-of-incidence and the sensor viewing geometry, it is possible to calibrate the remote sensor data to extract useful biophysical information.

Bidirectional Reflectance Distribution Function (BRDF): Early measurements of bidirectional reflectance obtained over various vegetation and soil surfaces demonstrated that most terrestrial surfaces exhibit non-Lambertian (*anisotropic*) reflectance characteristics (Kimes, 1983). In the past, bidirectional reflectance effects of the land surface did not play a major role in global change and ecological analysis, although they are assumed to be crucial for multi-temporal studies with varying Sun incidence angles. This was mainly due to a lack of bidirectional data available from remote sensors or acquired in field campaigns. The impact of the bidirectional reflectance distribution function is still not well understood despite the fact that we know it exists in much of the remotely sensed data commonly used for Earth
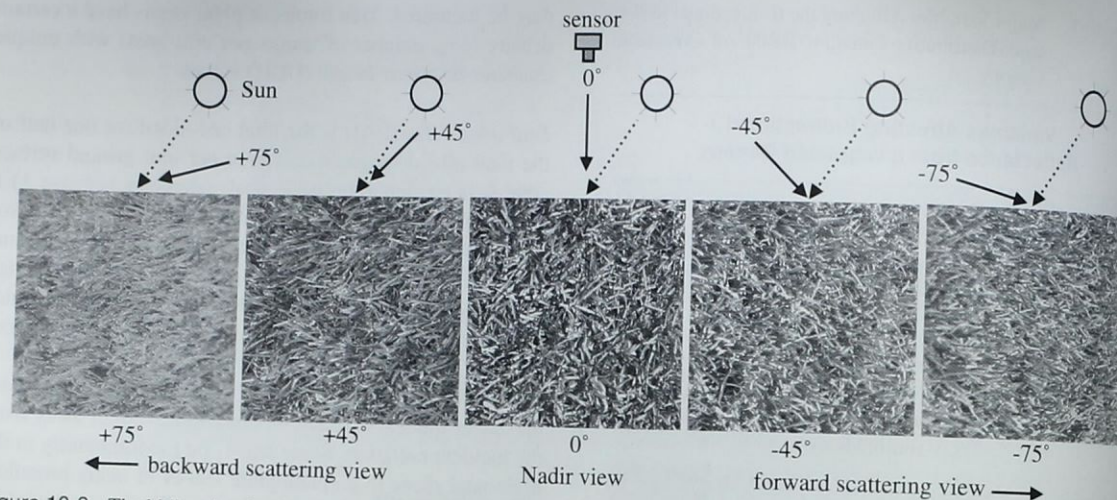
Figure 10-8   The bidirectional reflectance effect on a field of ryegrass (*Lolium perenne L.*) observed under different viewing angles in the solar principal plane from a FIGOS mounted camera. Solar zenith angle was at 35° as indicated by the dashed arrows. The sensor viewing angles are shown as black lines at nadir (0°) and at ±45° and ±75° off-nadir (after Sandmeier and Itten, 1999).

observation, especially for sensors with large fields of view such as the NOAA AVHRR 1.1 x 1.1 km data. A great amount of data from sensors with off-nadir viewing capability is becoming available, especially from commercial satellites such as Space Imaging's IKONOS, and NASA's *Terra* MODIS and MISR (Chapter 7). To properly apply these data in land-use change and ecologically relevant studies, the BRDF should be well understood to calibrate the data (Walter-Shea and Biehl, 1990; Abuelgasim et al., 1998).

Most terrain surfaces (soil, vegetation, and even water) reveal a relationship between the amount of reflected radiance, and 1) the geometric characteristics of the Sun's irradiance, and 2) the sensor viewing geometry. Hence the term *bidirectional*. Depending upon the specific irradiance and sensor viewing angles, most surfaces appear brighter or darker. We have all witnessed this effect. If we walk around a patch of grass or a pool of deep water, it may appear brighter or darker depending upon our viewing angle in relation to the constant incident angle of the Sun. For example, Figure 10-8 depicts a portion of a ryegrass lawn (*Lolium perenne L.*) illuminated by sunlight with a constant solar zenith angle of 35°. Individual photographs of the same grass canopy are obtained at nadir (0°) and at ±45° and ±75° off-nadir (Sandmeier and Itten, 1999). The terrain is generally brighter when the sensor records back-scattered energy as opposed to forward-scattered energy as the diagram reveals (i.e., the image on the left produced by the +75° back-scattered energy appears to be the brightest). Note,

however, that the +75° and -75° images are both much brighter than the image acquired at nadir, 0°.

The bidirectional effect in remote sensing data is most obvious when the angle of illumination and sensor viewing angle are nearly identical and in the same plane. This can produce a *hot spot* (i.e., a shadow is not visible). The solar principal plane is formed when the source, target, and the sensor are in the same plane (in the solar azimuth angle). This is where the BRDF effects are most pronounced. An example of a hot spot in aerial photography is shown in Figure 10-9.

Fortunately, scientists have developed instruments to measure the bidirectional reflectance distribution function of various surfaces. One of the most useful instruments is the *goniometer*. Here we briefly review the field goniometer system (FIGOS) designed by S. Sandmeier. FIGOS consists of a computer-controlled GER 3700 spectroradiometer sensitive to the wavelength interval from 300 – 2,450 nm in 704 bands with a spectral resolution of 1.5 nm for the interval 300 – 1,050 nm and 8.4 nm for the interval 1,050 – 2,450 nm. It consists of three major parts: a zenith arc rail, an azimuth rail, and a motorized sled where the radiometer is mounted (Figure 10-10a,b). The aluminum goniometer weighs approximately 230 kg and may be transported to field sites as shown. Mounted on the goniometer, the sensor views an area in the very center of the circle approximately 10.5 cm in diameter at nadir and about 41 cm (major axis) in the most extreme view zenith angle position of 75°.
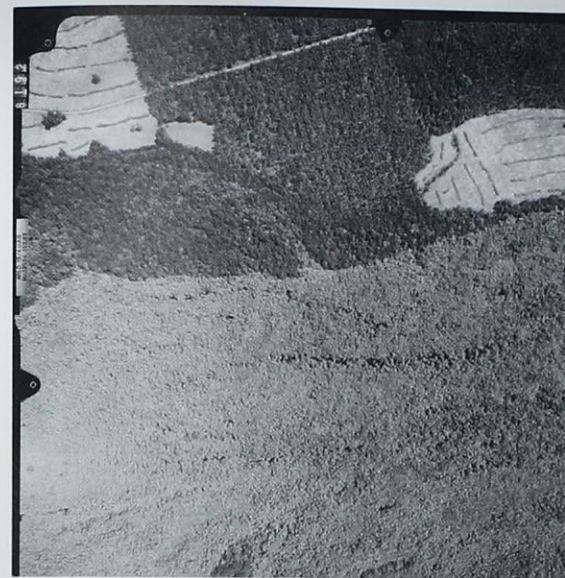

Figure 10-9   A hot spot near the left fiducial mark on a vertical aerial photograph of the Savannah River swamp in South Carolina. The Cypress-Tupelo forested wetland has relatively uniform percent canopy closure in this area. Its tone and texture should appear relatively homogeneous but they do not. A hot spot is produced when the angle of illumination and sensor viewing angle are nearly identical and in the same plane.

Thus, it is possible in a very short period of time while the Sun is approximately in the same zenith arc (θ_i) and azimuth (φ_i), to vary the position of the radiometer to determine if the amount of radiant flux in very specific wavelength regions (e.g., blue, green, red, near-infrared, middle-infrared) leaving the target is influenced by the sensor angle-of-view (θ_r) and azimuth (φ_r). If it is not, then we do not have to worry about BRDF effects. If the reflectance results are not uniform as will be demonstrated, then we may need to concern ourselves with adjusting for BRDF effects if we want to compare remote sensor data obtained on multiple dates (with varying Sun azimuth and zenith angle) or by sensors with multiple look angles (e.g., SPOT data acquired at 0° nadir on day 1 and 20° off-nadir on day 2).

The *bidirectional reflectance distribution function* (BRDF), f_r (sr⁻¹), is formally defined as the ratio of the radiance dL_r (W m⁻² sr⁻¹ nm⁻¹) reflected in one direction (θ_r, φ_r) to the Sun's incident irradiance dE_i (W m⁻² nm⁻¹) from direction (θ_i, φ_i) (Sandmeier, 1999; Sandmeier and Itten, 1999):

$$f_r(\theta_i, \varphi_i; \theta_r, \varphi_r; \lambda) = \frac{dL_r(\theta_i, \varphi_i; \theta_r, \varphi_r; \lambda)}{dE_i(\theta_i, \varphi_i; \lambda)}. \quad (10\text{-}6)$$

Note that dL_r and dE_i are directional quantities measured in solid angle steradians (sr⁻¹) as shown in Figure 10-10c.

Normally, a *bidirectional reflectance factor* (BRF, also referred to as R) is computed which is the radiance dL_r reflected from a surface in a specific direction divided by the radiance dL_{ref} reflected from a loss-less Lambertian reference panel measured under identical illumination geometry (Sandmeier and Itten, 1999):

$$R(\theta_i, \varphi_i; \theta_r, \varphi_r; \lambda) = \quad (10\text{-}7)$$

$$\left[\frac{dL_r(\theta_i, \varphi_i; \theta_r, \varphi_r; \lambda)}{dL_{ref}(\theta_i, \varphi_i; \theta_r, \varphi_r; \lambda)} \right] \times R_{ref}(\theta_i, \varphi_i; \theta_r, \varphi_r; \lambda)$$

where R_{ref} is a calibration coefficient determined for the spectral reflectance panel. Bidirectional reflectance factors (BRF) are dimensionless. Both BRF and BRDF take on values from zero to infinity. Values > 1 for BRF and > 1/π for BRDF are obtained in peak reflectance directions, such as the hot spot, where the reflected flux from a target surface is higher than the flux from a Lambertian surface.

It is also possible to develop an *anisotropy factor* which is used to analyze the spectral variability in BRDF data. Anisotropy factors (ANIF) allow separation of spectral BRDF effects from the spectral signature of a target. They are calculated by normalizing bidirectional reflectance data R to nadir reflectance, R_o (Sandmeier et al., 1998a; Sandmeier and Itten, 1999):

$$ANIF(\theta_i, \varphi_i; \theta_r, \varphi_r; \lambda) = \frac{R(\theta_i, \varphi_i; \theta_r, \varphi_r; \lambda)}{R_o(\theta_i, \varphi_i; \lambda)}. \quad (10\text{-}8)$$

So what do these measurements tell us about the BRDF of a typical surface? To answer this question, consider the nadir-normalized BRDF data (i.e., the ANIF data) of perennial ryegrass (*Lolium perenne L.*) shown in Figure 10-10d. During goniometer data collection the Sun zenith angle was 35°. Spectral results from four of the 704 possible spectroradiometer bands are presented using just the viewing zenith angle in the solar principal plane. It reveals that BRDF effects were very pronounced in the blue (480 nm) and red (675 nm) chlorophyll absorption bands previously discussed, whereas in the green and particularly in the low absorbing near-infrared range, relatively low BRDF effects were observed. Thus, persons using remote sensor data might consider radiometrically adjusting the brightness values associated with the blue and red bands, but not necessarily the near-infrared bands
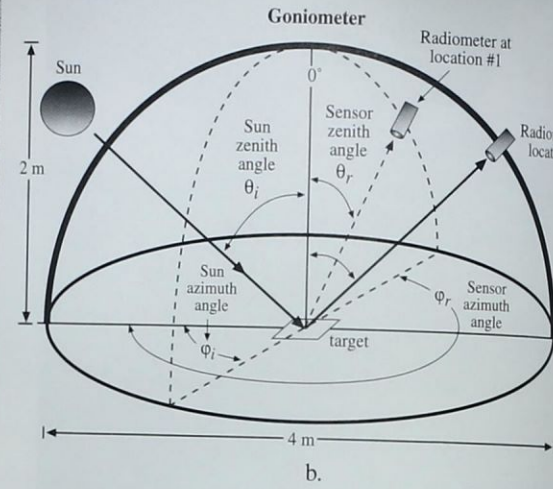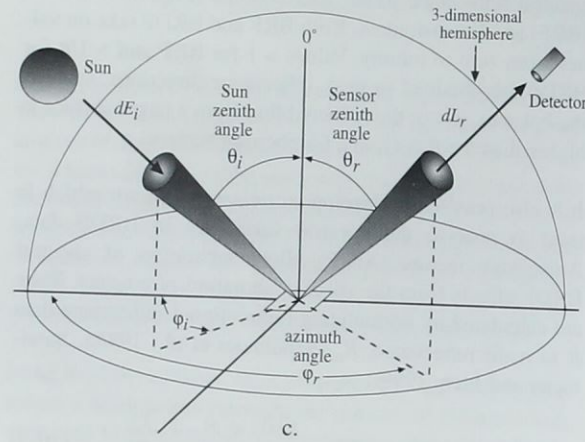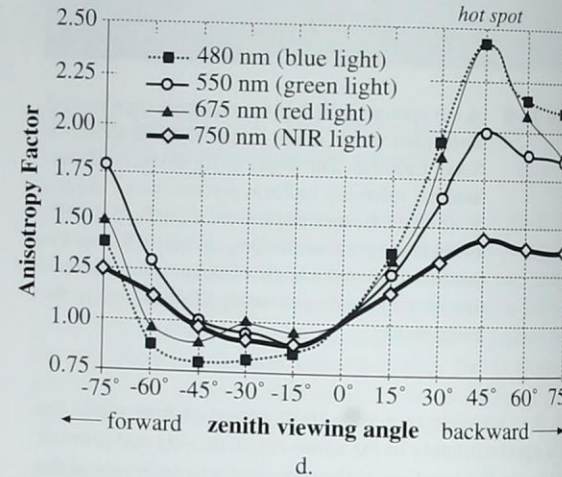
Figure 10-10 a) The field goniometer system (FIGOS) developed by S. Sandmeier. b) In this hypothetical example, the spectroradiometer is located at two locations. Spectral measurements are made at location #1 with a Sun zenith angle of θ_i and Sun azimuth angle of φ_i and a sensor angle of view of θ_r and azimuth angle of φ_r. The GER spectroradiometer records the amount of radiance leaving the target in 704 spectral bands. The radiometer is then moved to location #2 (i.e., perhaps only varying the sensor azimuth angle as shown) where it acquires radiance data again in 704 bands. c) The concept and parameters of the BRDF. A target is bathed in irradiance (dE_i) from a specific zenith and azimuth angle, and the sensor records the radiance (dL_r) exiting the target of interest at a specific azimuth and zenith angle. d) Anisotropy factor for ryegrass (Lolium perenne L.) at multiple zenith viewing angles in the solar principal plane for four of the 704 bands. The Sun zenith angle was 35° (after Sandmeier and Itten, 1999). e) Second generation Sandmeier Field Goniometer (SFG) obtaining smooth cordgrass (Spartina alterniflora) readings at North Inlet, SC, on October 21, 1999 (Sandmeier, 1999; Schill et al., 2000).
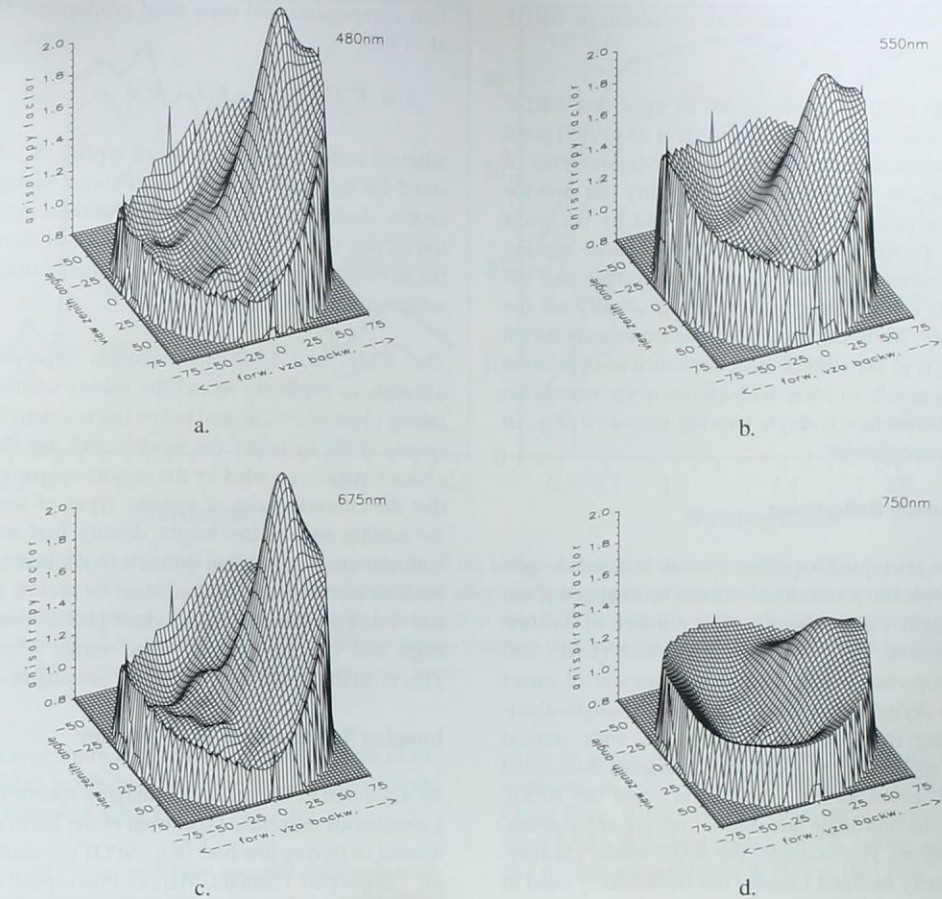
Figure 10-11 Anisotropy factors (nadir-normalized BRDF data) of ryegrass (Lolium perenne L.) for four spectral bands acquired with the FIGOS instrument with a Sun zenith angle of 35° (after Sandmeier and Itten, 1999).

under investigation. Typical for vegetated surfaces, all four bands exhibit a bowl shape, hot spot, and forward-scattering component.

It is actually more interesting to view the ryegrass anisotropy factors for the four wavelengths of interest according to not only the viewing zenith angle of 0° but in a range from ±75° (Figure 10-11). Ideally, the entire three-dimensional surface should be relatively flat as with the 750 nm near-infrared example, meaning that measurements in this specific band are relatively free of BRDF effects. Conversely, the 480 nm and 675 nm bands exhibit significant anisotropy factors. In the high-absorbing (i.e., low-reflecting) wavelength ranges, multiple scattering effects are reduced due to the relatively low amount of radiation in the canopy. Thus, the contrast between shadowed and illuminated canopy components are enhanced, which then enhances the BRDF effects. BRDF effects are rather small in the low-absorbing (i.e., high-reflecting) green and near-infrared wavelength ranges where multiple scattering effects are strong and diminish the contrast in the canopy (Sandmeier et al., 1998b).

Future field research using goniometers coupled with off-nadir pointing aircraft and satellite remote sensing systems such as Terra MISR (Chapter 7) will eventually document when we should be concerned with BRDF effects. Such information may help us 1) identify and select the bands that are impacted the least by BRDF effects, 2) recognize that there are certain Sun and/or sensor angle-of-view relationships that should be avoided when collecting remotely

sensed data, and/or 3) provide us with methods to radiometrically adjust the remote sensor data to minimize BRDF effects.

One should be careful, however, not to infer that BRDF effects are all bad. Strahler (1994) and Qi et al. (1995) point out that multidirectional remote sensing measurements of the terrain (e.g., at viewing angles off-nadir) can provide complementary information to that provided by the nadir measurement. In fact, a single nadir view remote sensing measurement obtains information about the surface as if the surface had no vertical structures, which is usually not the case in practice, while off-nadir view measurements reveal different aspects of the vertical structures such as vegetation height. *Consequently, to objectively characterize vegetation biophysical parameters, a single viewing geometry (e.g., at nadir) may be insufficient.*

Modeling Canopy Reflectance

Scientists have attempted to predict exactly how much radiant energy in specific wavelengths should be exiting a given leaf or vegetated canopy based on a number of factors, including (Danson, 1998): the leaf-area-index (LAI), soil reflectance properties below the canopy, amount of direct and/or diffuse skylight onto the canopy, the leaf-angle-distribution (ranging from erectophile canopies with vertical leaves at 90° inclination to planophile canopies dominated by horizontal leaves with 0° inclination), and the BRDF influenced by the Sun angle and sensor viewing angle geometry just discussed. For example, the SAIL model (Scattering by Arbitrarily Inclined Leaves) has been widely used in remote sensing research for investigating the spectral and directional reflectance properties of vegetation canopies. It uses radiative transfer equations to model energy interacting with a vegetation canopy in three distinct streams, including a downward flux of direct radiation and a downward and upward flux of diffuse radiation (Verhoef, 1984; Goel, 1988). It assumes that the canopy may be represented by small absorbing and scattering elements (e.g., leaves) with known optical properties, distributed randomly in horizontal layers and with known angular distribution. The model has been used to simulate the effects of off-nadir viewing, to simulate spectral shifts of the red-edge, and to estimate canopy properties directly from remotely sensed data (Jacquemoud et al., 1995).

Similarly, the Li-Strahler model (1985; 1992) yields estimates of the size and density of trees from remotely sensed images. The signal received by the sensor is modeled as consisting of reflected light from tree crowns, their shadows, and the background within the field of view of the sensor.

The reflected signal is modeled as a linear combination of four components and their areal proportions (Woodcock et al., 1997):

$$S = K_gG + K_cC + K_tT + K_zA \qquad (10\text{-}9)$$

where S is the brightness value of a pixel, K_g, K_c, K_t, and K_z stand for the areal proportions of sunlit background, sunlit crown, shadowed crown, and shadowed background, respectively, and G, C, T, and A are the spectral signatures of the respective components. This is called a mixture model, or a scene component model.

The SAIL and Li-Strahler models represent important attempts to explicitly model the energy-matter interactions taking place above, in, and below the vegetative canopy. Scientists strive to invert the models and use the reflectance characteristics recorded by the remote sensor system to predict the characteristics of specific types of structure within the canopy, such as tree height, density, leaf-area-index, etc. Unfortunately, it is often difficult to calibrate such models because so much information must be known about the leaf and canopy characteristics, atmospheric conditions, Sun angle and viewing geometry, and terrain slope and aspect. This is an important area of remote sensing research.

Imaging Spectrometry of Vegetation

As discussed in Chapter 7, an imaging spectrometer collects a continuous reflectance spectrum of the Earth's surface. But instead of having just four (e.g., SPOT) or eight (e.g., Landsat 7 Enhanced Thematic Mapper Plus) spectral channels to characterize the vegetation spectral characteristics, an imaging spectrometer records information in hundreds of spectral channels.

Imaging spectrometry has great potential for monitoring vegetation type and biophysical characteristics (Goetz, 1995). Vegetation reflectance spectra are often quite informative, containing information on the vegetation chlorophyll absorption bands in the visible region, the sustained high reflectance in the near-infrared region, and the effects of plant water absorption in the middle-infrared region.

Geologists have been using hyperspectral imagery for years to discriminate between different rock types based on their spectral reflectance and absorption characteristics. They have prepared an exhaustive spectral library of the most important minerals, soils, and rock types (e.g., Clark et al., 1993). When calibrated airborne hyperspectral imagery are acquired, they often compare the spectra obtained from the airborne data to the spectra stored in the database to deter-
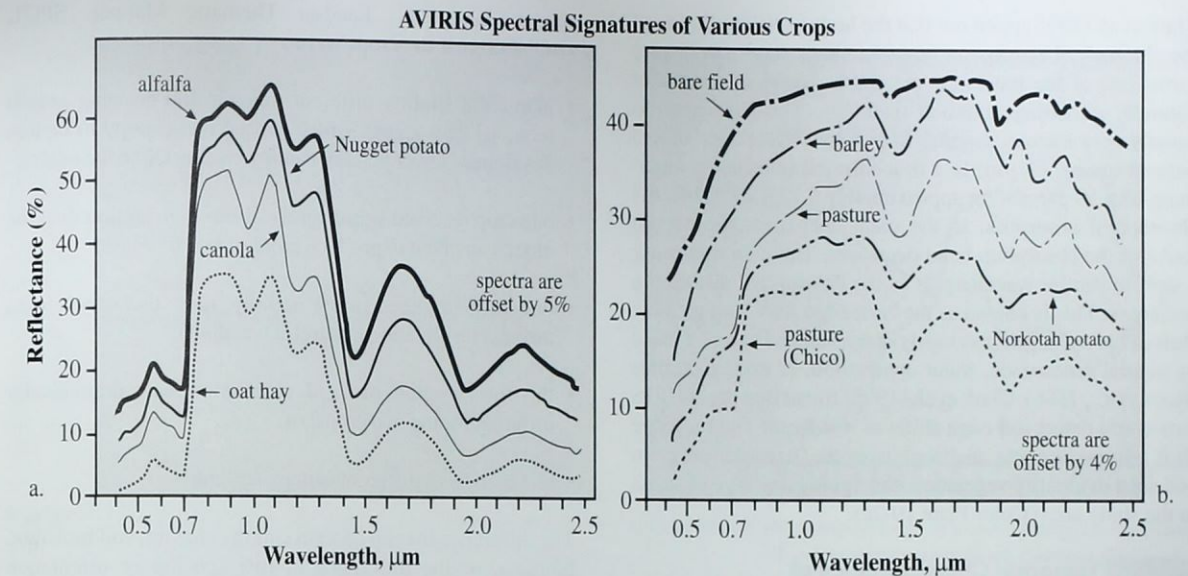

AVIRIS Spectral Signatures of Various Crops

Figure 10-12 a) Spectra of healthy green vegetation in the San Luis Valley of Colorado obtained on September 3, 1993, using AVIRIS; 224 channels at 20 × 20 m pixels. b) Most of these other vegetation types exhibited reduced chlorophyll absorption effects. Note that the spectra are offset for clarity (after Clark et al., 1995). Differences in the reflectance and/or absorption characteristics of the vegetation make it possible in certain instances to distinguish one vegetation type from another or to identify if the vegetation is undergoing stress by some agent.

mine mineral type and other characteristics. Several examples are provided in Chapter 13 (Remote Sensing of Soils, Minerals and Geomorphology).

Ideally, there would be a vegetation spectral databank available that contains information on: 1) the spectral reflectance and emittance characteristics of every type of vegetation in the region from 0.35 – 14 μm, 2) how these data appear on different dates throughout the pertinent growing seasons, and 3) what these spectra should look like in the event of stress or insect infestation. Unfortunately, such a database does not yet exist. Instead, it is still usually necessary to collect *in situ* spectroradiometer data of the vegetation of interest at the time of the overflight and then use this data to calibrate the spectral reflectance information derived from the airborne spectroradiometer. When this is performed carefully, it is possible to extract vegetation type and condition information from the hyperspectral data.

For example, consider the AVIRIS data collected over the San Luis Valley of Colorado on September 3, 1993, shown in Color Plate 10-2a (Clark et al., 1995). The 224 spectral channels of 20 × 20 m AVIRIS data were radiometrically corrected to remove the effects of atmospheric water vapor and geometrically rectified to a standard map projection. Land

cover of some of the fields at the time of the overflight are annotated in color on top of the single AVIRIS channel in Color Plate 10-2a. AVIRIS reflectance spectra for some of these fields, including potato, alfalfa, barley, oat hay, canola, and pasture are portrayed in Figure 10-12a,b.

The alfalfa, canola, oat hay, and Nugget potato spectra show the plants to be green and healthy (Figure 10-12a). Barley had lost all of its chlorophyll response at the time of the overflight (Figure 10-12b). Norkotah potatoes were not being irrigated as they were about to be harvested, and consequently they show weak chlorophyll and cellulose absorptions, with soil (clay) absorption from exposed soil. Field investigation revealed that the potatoes were also being sprayed with a defoliant. Thus, they exhibit decreased chlorophyll absorption along with a shift of the red-edge to shorter wavelengths as we would expect. The Chico and pasture spectra exhibit combinations of chlorophyll and cellulose (dry vegetation) absorption. The spectra from the known fields was used in a special computer program called *Tricorder,* developed at the U.S. Geological Survey, to identify other pixels in the study area with similar spectral response (Clark et al., 1995). The result was a classification map that was approximately 96 percent accurate (Color Plate 10-2b).

Clark et al. (1995) point out that the long-wavelength side of the chlorophyll absorption (approximately 0.68 – 0.73 μm) forms one of the most extreme slopes found in spectra of naturally occurring common materials. The absorption is usually very intense, ranging from a low reflectance of < 5 percent (near 0.68 μm) to a near-infrared reflectance maximum of ≥ 50 percent (at approximately 0.73 μm). When the chlorophyll absorption in the plant decreases, the overall *width* of the absorption band decreases. These factors cause a shift to shorter wavelengths as the chlorophyll absorption decreases. This is known as the "red-edge shift" or the "blue shift of the red edge" previously discussed and can be caused by natural senescence, water deprivation, or toxic materials (Rock et al., 1986). Clark et al. (1995) found that the AVIRIS data could detect red-edge shifts of < 0.1 nm. The red-edge shift information was analyzed using the Tricorder program and used to identify vegetation undergoing any type of stress in the study area (Color Plate 10-2c).

Temporal Characteristics of Vegetation

Timing is very important when attempting to identify different vegetation types or to extract useful vegetation biophysical information (e.g., biomass, chlorophyll characteristics) from remotely sensed data. Selecting the most appropriate date(s) for data collection requires an intimate knowledge of the plants' temporal *phenological* (growth) *cycle*. Plants whose leaves drop seasonally are *deciduous*. Plants whose leaves remain from season to season are *evergreen*.

A noted remote sensing scientist, Dave Simonett, often said "Green is green is green." By this he meant that if two different crops (e.g., corn and cotton) were planted at the same time and had complete canopy closure on the same date as the remotely sensed data were collected, the spectral reflectance characteristics of the two crops would most likely appear to be very similar throughout the visible and near-infrared portion of the spectrum. His comment was based on the use of the relatively broad-band sensors available in the 1970s and 1980s. We now have hyperspectral sensors that allow us to sample in relatively narrow portions of the spectrum, hopefully identifying unique absorption features that will allow us to discriminate between one vegetation type and another or to extract biophysical information.

Nevertheless, Simonett's observation is still correct in many instances. Often our only hope of discriminating between two crops using relatively coarse spectral resolution remote

sensor data (e.g., Landsat Thematic Mapper, SPOT, IKONOS) is if the crops were:

- planted at slightly different times in the growing season (e.g., 10 days apart), which caused one canopy to be less developed (lower percent canopy closure) than the other;

- one crop received significantly different irrigation than the other, causing it to produce more or less biomass;

- one crop matured more rapidly than the other (e.g., through fertilization or careful weeding);

- the row spacing or field orientation was dramatically different for the two crops; or

- one crop has a different canopy structure.

The difference in crop percent canopy closure, soil moisture, biomass, or the difference in row spacing or orientation might cause one crop to have dramatically different reflectance properties due to the influence of the background soil or understory materials present. Therefore, it is often the proportion of background material present within the instantaneous field of view of the sensor system (e.g., perhaps 1 x 1 ft for high resolution color-infrared aerial photography; 30 x 30 m for Landsat Thematic Mapper imagery) that allows us to discriminate between the two vegetation types. The amount of understory background material present is largely a function of the stage of the plant in its phenological cycle. Therefore, if a scientist is trying to differentiate (classify) between several crops, wetland, or forest types using remote sensor data, it is essential to know the phenological cycle characteristics of all of them. This information is then used to determine the optimum time of year to collect the remotely sensed data to discriminate one land cover or vegetation type from another.

Another important temporal factor cannot be overlooked. Plants require water to grow. Therefore, their most productive growth period is often associated with the most intense periods of precipitation and associated cloud cover. For example, Figure 10-13 identifies the annual percent cloud cover statistics for several areas in the United States. Except for California, with its low humidity and low cloud cover, most of the areas have their greatest cloud cover at exactly the time when scientists may want to collect the maximum amount of remote sensor data during the growing season. Consequently, scientists must juggle the identification of the optimum date of remote sensor data using the phenological calendar with the likely spectre of considerable cloud cover
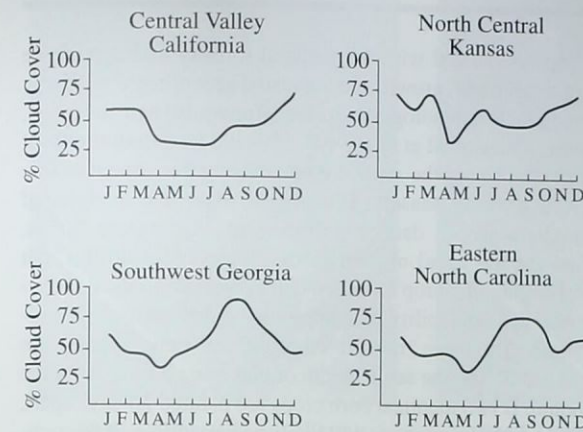

Figure 10-13 Predicted percent cloud cover in four areas in the United States. The greatest amount of cloud cover is often associated with the height of the growing season, except for California. This can significantly complicate the collection of remote sensing data for vegetation analysis.

being present. This is why we need higher temporal resolution sensors.

The development of forests, grassland, and wetland canopies follow relatively predictable cycles each year except when they are under stress from a pathogen or when unseasonably high or low temperatures occur. Similarly, all managed agricultural crops have relatively well-known phenological cycles within a given region, but these may be modified by individual farmers. Therefore, it is useful to review the phenological cycles of both natural vegetation systems and managed agricultural systems to gain insight into how important the cycles are when using remote sensing to extract vegetation biophysical information. Several case studies are provided.

Natural Phenological Cycles

Many plant species found in forests, wetland, rangeland, etc., have relatively unique phenological growth cycles (Yool et al., 1997). They leaf-out, grow to maturity, and senesce at approximately the same time each year. However, unseasonably cold or warm temperatures in the spring or fall can shift their annual phenological cycles by as much as 30
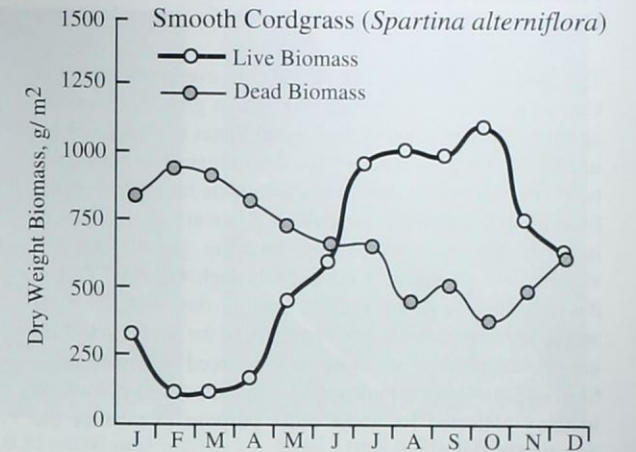
Figure 10-14 Phenological cycle of Smooth Cordgrass (*Spartina alterniflora*) biomass in South Carolina. The greatest amount of live biomass is present from July through October. The greatest amount of dead biomass is present from January through March. The marsh contains approximately equal proportions of live and dead biomass in December and June (after Dame and Kenny, 1986; Jensen et al., 1998).

days. Therefore, the analyst must be aware of whether the remotely sensed data were collected in a typical or atypical year. If a scientist is attempting to classify vegetation using remote sensor data, it is often wise to collect the data early in the growing season when the vegetation is developing at different rates, which yield different percent canopy closures, hopefully creating differences in their spectral signatures. For example, if one is attempting to discriminate among various inland wetland species (e.g., cattail, willow, buttonbush) in the southeastern United States, it is best to collect imagery from February 15 through May 1. After May 1, most of the wetland vegetation has achieved complete canopy closure, and the spectral signatures of the various canopies become similar, i.e., "Green is green is green."

Conversely, if the goal is to monitor the biomass of the vegetation, it is useful to collect remote sensor data at the height of the growing season when the maximum biomass exists. Monitoring biomass through time can provide important information about the stability of the natural ecosystem and whether significant change is taking place. The following section demonstrates this logic applied to monitoring coastal Smooth Cordgrass wetland (Figure 10-14).

Phenological Cycle of Coastal Smooth Cordgrass in South Carolina

The annual phenological cycle of evergreen Smooth Cordgrass (*Spartina alterniflora*), which grows extensively along the eastern coast of the United States is shown in Figure 10-14. The decomposed *Spartina* organic matter (detritus) is carried out to sea and represents the foundation of the food chain that supports the Eastern Seaboard marine fishery industry. The time of greatest *Spartina* growth and dry weight biomass occurs from July through October. This is the optimum time for remote sensing data collection. It serves little purpose to obtain imagery of the *Spartina* in January through March, when it is in a senesced (dormant) state. Still, one often encounters persons who attempt to use winter imagery collected for some other purpose to monitor the *Spartina* wetland.

Figure 10-15 displays nine bands of 3 x 3 m NASA Calibrated Airborne Multispectral Scanner (CAMS) data of Murrells Inlet, SC, obtained on August 2, 1997, during the high biomass time of year. *In situ* Smooth Cordgrass total dry biomass (g/m^2) measurements were obtained at 27 locations on August 2 and 3, 1997. The *in situ* data were then correlated with individual band brightness values and vegetation transforms of the original CAMS data (Jensen et al., 1998). One of the most impressive relationships was between the fundamental near-infrared band 6 CAMS data and the *in situ* measurements, which yielded a correlation coefficient of 0.88 and an r^2-value of 0.774 meaning that approximately 77 percent of the variance was accounted for (Figure 10-16).

Color Plate 10-3 is a map of the spatial distribution of total dry biomass for a small portion of Murrells Inlet on August 2, 1997. It was produced using the regression equation:

$$y = 3.4891x - 23.9 \qquad (10\text{-}10)$$

where *y* is total biomass (g/m^2) and *x* is the CAMS band 6 brightness value. Studies such as this provide important baseline biophysical information that can be compared against future studies to determine if deleterious changes in biomass are occurring in the inlet. Comparative biomass studies would require that most of the system and environmental variables remain constant (e.g., approximately the same sensor system configuration and viewing geometry, altitude above-ground-level, atmospheric conditions, anniversary date, time of day, and tidal cycle). The limitations of using a regression approach when predicting biophysical variables using remotely sensed data are summarized in Qi et al. (1995).

Managed Phenological Cycles

Crops associated with mechanized forestry and agriculture are established, grown, and harvested according to relatively predictable phenological cycles (Rundquist and Sampson, 1988; Thenkabail et al., 1994). It would be wonderful if all farmers planted the same crop on exactly the same date in a given growing season. This would make the analysis of remotely sensed data straightforward. Fortunately for us who eat the bread of their labors, they do not do this, but rather plant the crop based on current meteorological conditions, the availability of equipment, and heuristic rules-of-thumb. Therefore, not all crops of the same species are planted during the same month or harvested during the same month. If two identical corn crops are planted 20 days apart, their spectral signatures will likely be very different throughout their respective phenological cycles. This condition may cause problems when attempting to perform crop identification using remote sensor data.

County agricultural extension agents and land-grant university scientists know the local and regional crop phenological cycles very well. They often represent the most important sources for valuable crop phenology and soils information and any idiosyncrasies associated with local farming practices. It is instructive to provide examples of several agricultural phenological cycles that span the geography of the conterminous United States to demonstrate the importance of vegetation phenological information. This will include case studies concerning hard red winter wheat in the Midwest United States, several major crops in South Carolina, and remote sensing of sugar beets, cotton, and alfalfa in the Imperial Valley, CA. Each example includes detailed phenological information displayed in different formats.

Phenological Cycle of Hard Red Winter Wheat in the Midwest United States

The detailed phenological cycle of hard red winter wheat (*triticale*) grown on the prairie soils in the Midwest United States is shown in Figure 10-17. The crop is established in October and November. It lies dormant under snow cover (if present) until March, when growth resumes. Hard red winter wheat greens up in April and produces heads of grain in May. It matures by mid-June. It is usually ripe and harvested by early July. Remotely sensed data acquired in October and November provide information on the amount of land prepared during the crop establishment period. Imagery acquired during the green-up phase in April and May can be used to extract information on standing-crop biomass and perhaps predict the harvested wheat yield.

Band 1 (blue; 0.45 – 0.52 µm) Band 2 (green; 0.52 – 0.60 µm) Band 3 (red; 0.60 – 0.63µm)

Band 4 (red; 0.63 – 0.69 µm) Band 5 (near-infrared; 0.69 – 0.76 µm) Band 6 (near-infrared; 0.76 – 0.90 µm)

Band 7 (mid-infrared; 1.55 – 1.75 µm) Band 8 (mid-infrared; 2.08 – 2.35 µm) Band 9 (thermal-infrared; 10.4 – 12.5 µm)
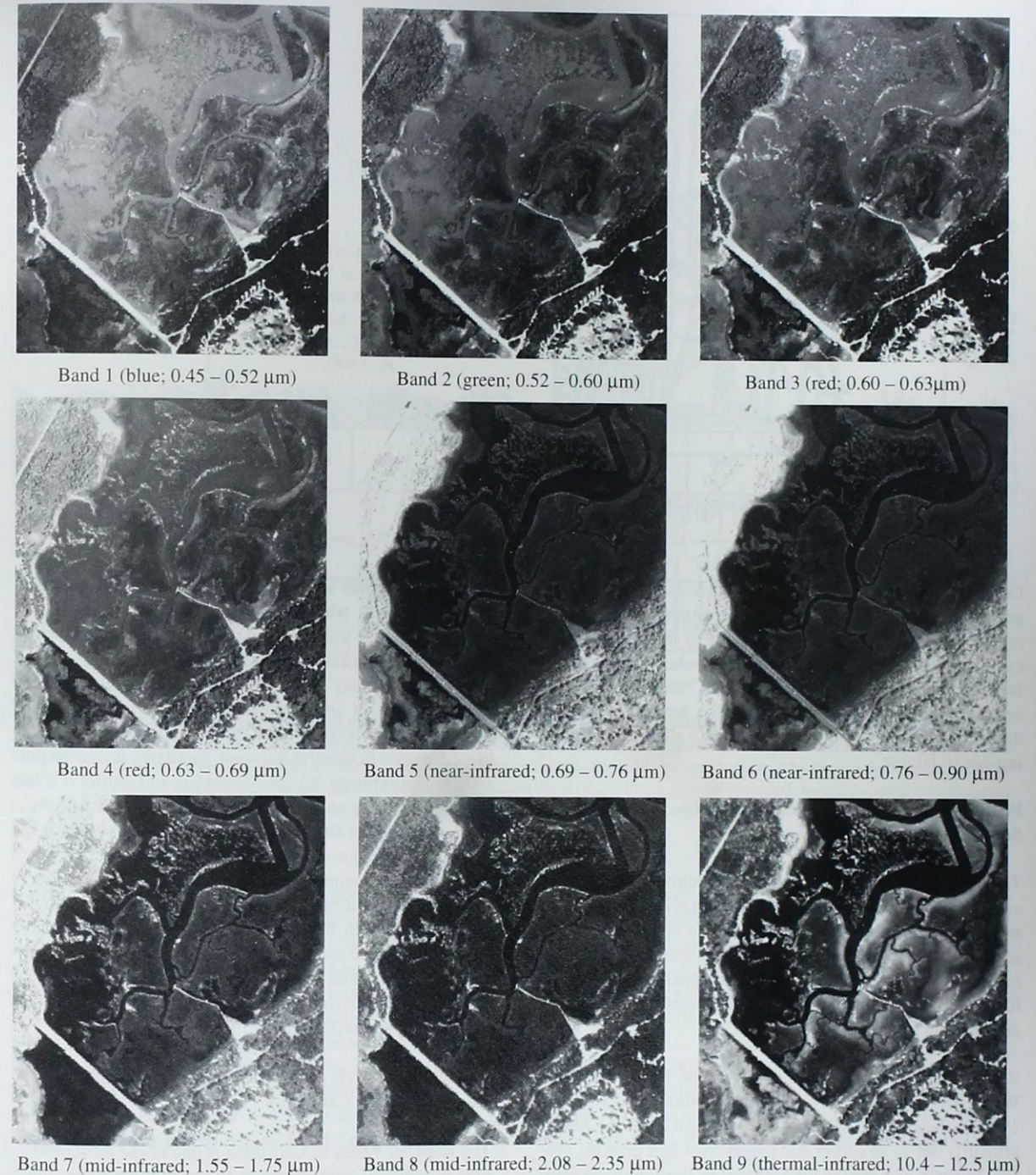
Figure 10-15 Nine bands of 3 x 3 m Calibrated Airborne Multispectral Scanner (CAMS) data of Murrells Inlet, SC, obtained on August 2, 1997. The data were obtained at 4,000 ft above-ground-level.
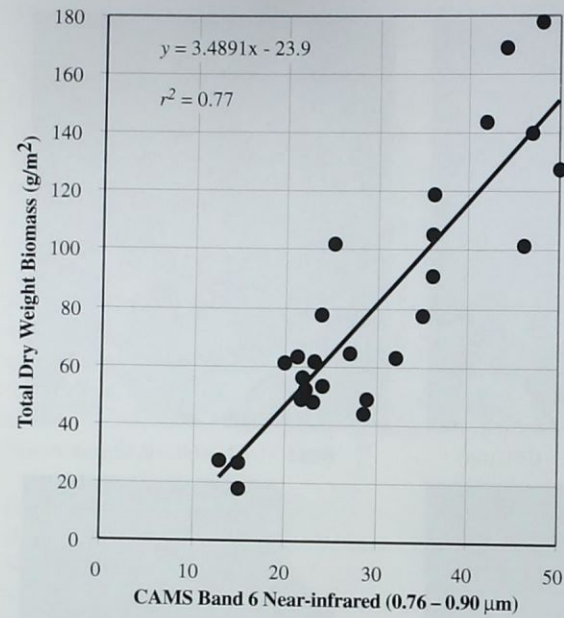
Figure 10-16 Relationship between Calibrated Airborne Multi-spectral Scanner (CAMS) band 6 brightness values and *in situ* measurement of *Spartina alterniflora* total dry biomass (g/m^2) at 27 locations in Murrells Inlet, SC, obtained on August 2 and 3, 1997 (Jensen et al., 1998).

Figure 10-17 The phenological cycle of hard red winter wheat in the Great Plains of the United States. The crop is established in October and November. It lies dormant under snow cover until March, when growth resumes. The plants green up in April, produce heads of grain in May, and mature by mid-June. The wheat is usually dead ripe and harvested by early July. Remotely sensed data acquired in October and November provide information on the amount of land prepared during the crop establishment period. Imagery acquired during the green-up phase in April and May can be used to extract information on standing-crop biomass and perhaps predict the harvested wheat yield.

Detailed crop calendar information such as this is used by governments, individuals, and private companies to acquire remote sensing data at optimum dates in the phenological cycle in order to model and predict the production of specific food for sale on the world market. Such monitoring may in certain instances also be used to predict future agricultural disasters due to severe drought, hopefully alleviating suffering due to famine.

Phenological Cycle of Agricultural Crops in South Carolina

The phenological cycles of natural and cultivated vegetation varies greatly by region. For example, if a scientist wanted to monitor the condition of the wheat crop in South Carolina, it is *not* possible to use the Midwest wheat phenological information presented in Figure 10-17. The phenological cycles for wheat and South Carolina's other major cash crops are presented in Figures 10-18 and 10-19.

Wheat heads in late May and early June in the Midwest. Wheat heads in early May in South Carolina, approximately 15 days ahead of the Midwest phenological cycle for wheat, primarily due to an earlier and longer frost-free growing season. Imagery acquired in the Midwest in June might be valuable for inventorying wheat production, whereas imagery obtained in June in South Carolina might well reveal that the wheat crop has already been harvested.

The crop calendars also reveal that it should be straightforward to identify wheat production in South Carolina by acquiring a single image in March or early April when wheat is the only crop in existence with a complete canopy closure. Conversely, it may be difficult to differentiate between tobacco and corn unless we obtain a mid-June image and hope that the tobacco is leafed out more than corn, resulting in a difference in spectral response. Similarly, it may be possible to discriminate between soybeans and cotton if a late July or early August date is selected and soybeans have a greater canopy closure than cotton. If all the phenological cycles of the major crops were exactly the same for South Carolina, with complete canopy closure at the same time of year, it would be difficult to use remotely sensed data to discriminate between the vegetation types. However, because their phenological cycles are staggered throughout the growing season to some degree, it is possible to discriminate between them if the imagery is collected at optimum times in the growing season (Savitsky, 1986).

Phenological Cycle of Agricultural Crops in the Imperial Valley, California

The Imperial Valley of California is one of the most productive agricultural ecosystems in the world, producing great quantities of sugar beets, cotton, and alfalfa. The phenological cycles of several of its major crops are summarized in Color Plate 10-4 (Byrd, 1998; GRSU, 1999). Each calendar

depicts a single field monitored throughout a 12-month period using 79 x 79 m Landsat Multispectral Scanner (MSS) data (RGB = bands 4,2,1). The brighter red (magenta) the signature, the greater the amount of biomass and crop canopy closure. Sugarbeets are established in early September, emerge in November, and are harvested in April and early May. By law, cotton must be planted in March and harvested and plowed under in November of each year to control Bole Weevil. In 1982, the plow-down date was January 1. Alfalfa is planted year-round and may be harvested five or six times per year as depicted in the crop calendar.

It is possible to identify the type of crop in each field if imagery is obtained at times of the year that maximize the spectral contrast between crops. For example, Figure 10-20

depicts seven bands of Landsat Thematic Mapper imagery obtained on December 10, 1982. Six of the bands are at 30 x 30 m, while the thermal infrared band (6) is at 120 x 120 m spatial resolution. A ground reference crop map provided by the Imperial Valley Irrigation Board is also included (Haack and Jampoler, 1995).

The four color composites shown in Color Plate 10-5 demonstrate the importance of the middle-infrared bands when attempting to discriminate among crop types. The fundamental visible (RGB = bands 3,2,1) and near-infrared color composites (RGB = bands 4,3,2) are not nearly as effective for visual determination of the crop types as the visible and middle-infrared composites (RGB = bands 5,3,2 and RGB = bands 7,3,2). Note that all the sugarbeet fields show up as

Soybeans　a.

125
100
75
50
25 cm height

100%
ground
cover

50%

JAN	FEB	MAR	APR	MAY	JUN	JUL	AUG	SEP	OCT	NOV	DEC

| Dormant or multicropped | Initial growth | Development | Maturity | Harvest | |

Corn　b.

300
250
200
150
100
75
50
25 cm height

100%

50%

JAN	FEB	MAR	APR	MAY	JUN	JUL	AUG	SEP	OCT	NOV	DEC

| Dormant or multicropped | 8-leaf | 12-14 leaf | Tassle | Blister | Dent/Harvest | Dormant or multicropped |

10 - 12 leaf

Figure 10-18 Phenological cycles of soybeans (a) and corn (b) in South Carolina (Savitsky, 1986).

Winter Wheat　a.

100
75
50
25 cm

100%
ground
cover

50%

JAN	FEB	MAR	APR	MAY	JUN	JUL	AUG	SEP	OCT	NOV	DEC

| Tillering | Jointing | Booting | Head | Harvest | Dormant or multicropped | Seed |

Cotton　b.

150
125
100
75
50
25 cm height

100%
ground
cover

50%

JAN	FEB	MAR	APR	MAY	JUN	JUL	AUG	SEP	OCT	NOV	DEC

| Dormant or multicropped | Seeding | Fruiting | Boll | Maturity/harvest | |

Pre-bloom

Tobacco　c.

125
100
75
50
25 cm height

100%

50%

JAN	FEB	MAR	APR	MAY	JUN	JUL	AUG	SEP	OCT	NOV	DEC

| Dormant or multicropped | Transplanting | Development | Maturity/harvest | Dormant or multicropped |

Topping

Figure 10-19 Phenological cycles of winter wheat (a), cotton (b), and tobacco (c) in South Carolina. The information was obtained from county agricultural extension agents, Clemson land-grant university extension personnel, and field work (Savitsky, 1986).

Band 1 (blue; 0.45 – 0.52 μm)   Band 2 (green; 0.52 – 0.60 μm)   Band 3 (red; 0.63 – 0.69 μm)

Band 4 (near-infrared; 0.76 – 0.90 μm)   Band 5 (mid-infrared; 1.55 – 1.75 μm)   Band 7 (mid-infrared; 2.08 – 2.35 μm)

Landsat Thematic Mapper Imagery of Imperial Valley, California, December 10, 1982

Sugarbeets   Cotton

Alfalfa   Fallow

Band 6 (thermal infrared; 10.4 – 12.5 μm)   Ground Reference

Figure 10-20 Individual bands of Landsat Thematic Mapper imagery of a portion of the Imperial Valley, CA, obtained on December 10, 1982. Bands 1 – 5 and 7 have a spatial resolution of 30 x 30 m. Band 6 has a spatial resolution of 120 x 120 m. Sugarbeets are bright in the near-infrared band 4 data and dark in both the middle-infrared bands (5 an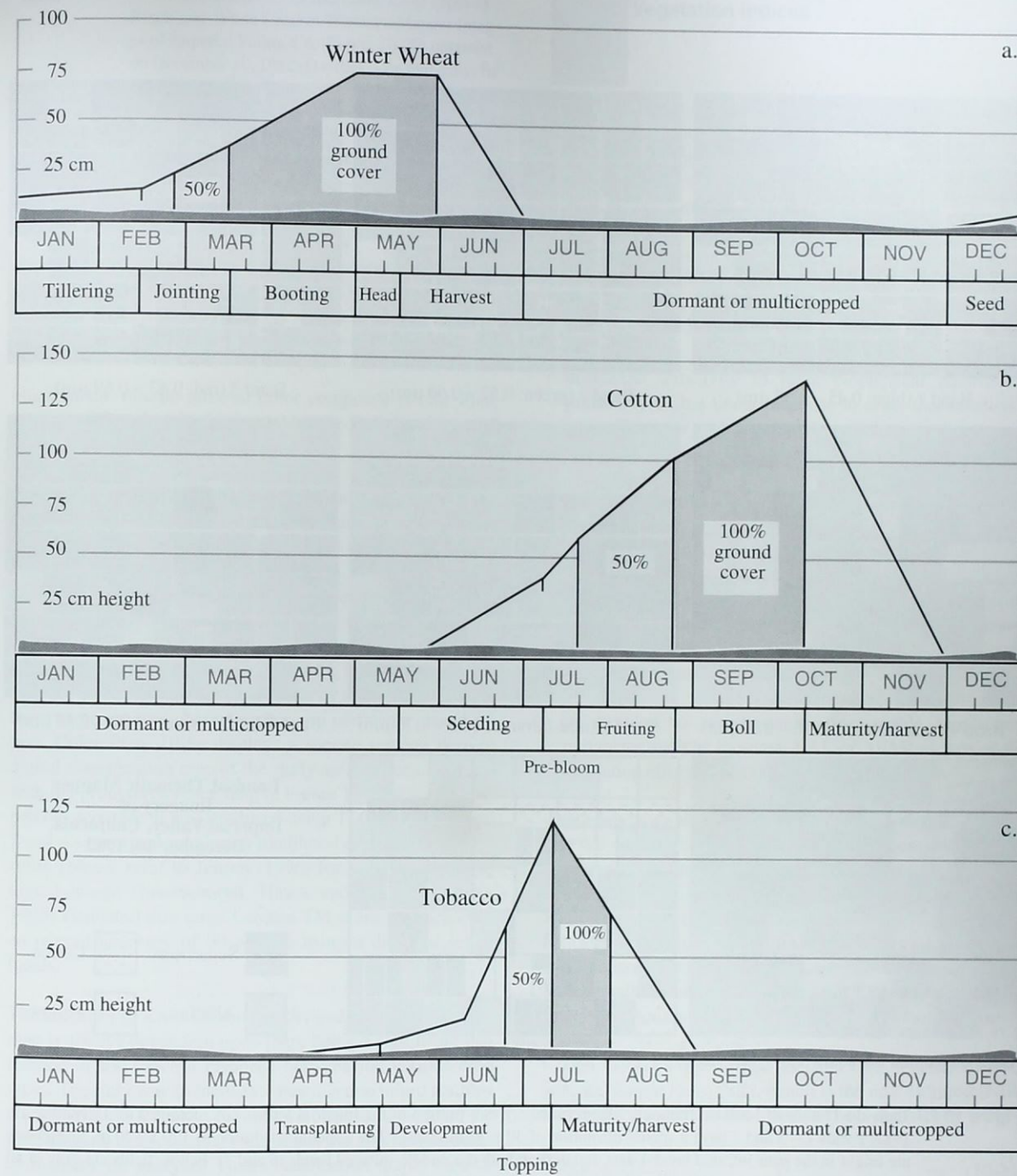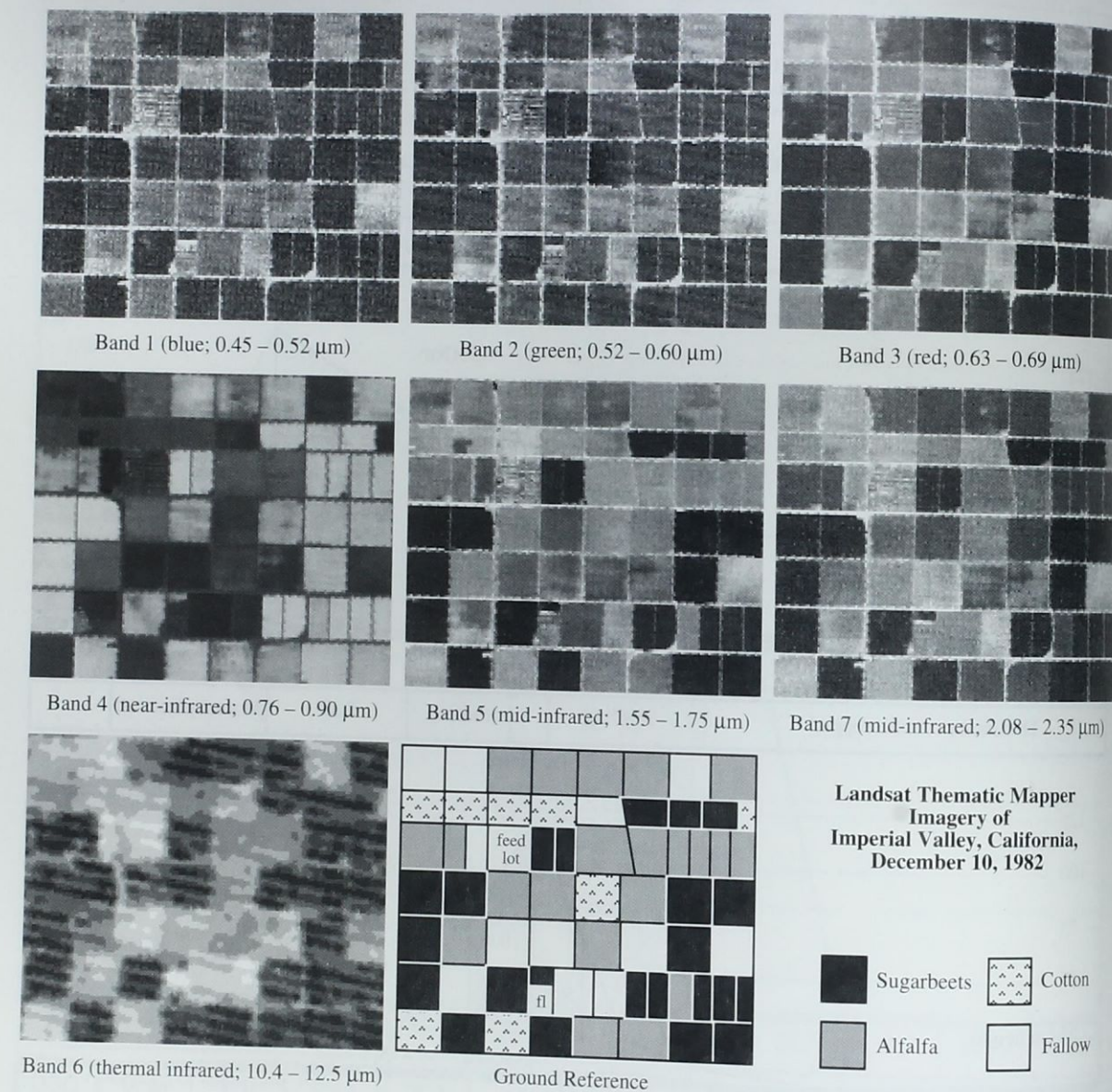d 7). Fallow fields are gray in all bands except band 4 (near-infrared), which is dark (images courtesy of Space Imaging, Inc.).

Table 10-2.   Tonal Characteristics of Individual Crop Types in Black-and-White Landsat Thematic Mapper Images of Imperial Valley, CA (Figure 10-20) obtained on December 10, 1982 (D = dark; G = mid-gray; Br = brighter)

Crop Type	TM1	TM2	TM3	TM4	TM5	TM7
Sugarbeets	D	D	D	Br	D	D
Alfalfa	D	D	D	Br	G	G
Cotton	G	G	G	D	Br	Br
Fallow land	G	G	G	D	G	G

black in the middle-infrared color composite (Color Plate 10-5c; RGB = bands 5,3,2) and in the individual band 5 image (Figure 10-20).

Because of the significant spectral contrast among the crops in this December 10, 1982, Landsat TM image, it is possible to perform a visual classification of the crops based on an examination of the individual bands in Figure 10-20. For example, after careful examination we see that the heuristic rules summarized in Table 10-2 could be used to classify the scene.

It is also possible to program a computer to take into account these same spectral characteristics and perform a classification. Color Plate 10-5e displays a remote sensing derived digital classification map of the study area. When compared with the ground reference map in Figure 10-20 it is about 85 percent accurate. It was produced using TM bands 1 – 5 and 7 and a supervised maximum likelihood classification algorithm [please refer to Jensen (1996) for information about digital image classification]. Haack and Jampoler (1994; 1995) evaluated this same Landsat TM scene and achieved an overall accuracy of 90 percent using a different set of bands.

The accuracy of a remote sensing derived crop classification map is always dependent upon there being a significant difference in the spectral response between the various crop types. The only way to identify when this maximum contrast among spectral response should take place is to evaluate the phenological crop calendars and select the appropriate dates of imagery for analysis. Then classification maps, such as the one shown in Color Plate 10-5, can be used to predict the amount of acreage in specific crops at a given instant in time. Such information coupled with agricultural-meteorological models can be used to predict crop yield.

Vegetation Indices

Since the 1960s, scientists have extracted and modeled various vegetation biophysical variables using remotely sensed data. Much of the effort has gone into the development of *vegetation indices* — defined as dimensionless, radiometric measures that function as indicators of relative abundance and activity of green vegetation, often including leaf-area-index (LAI), percentage green cover, chlorophyll content, green biomass, and absorbed photosynthetically active radiation (APAR). A vegetation index should (Running et al., 1994; Huete and Justice, 1999):

- maximize sensitivity to plant biophysical parameters, preferably with a linear response in order that sensitivity be available for a wide range of vegetation conditions, and to facilitate validation and calibration of the index;

- normalize or model external effects such as Sun angle, viewing angle, and the atmosphere for consistent spatial and temporal comparisons;

- normalize internal effects such as canopy background variations, including topography (slope and aspect), soil variations, and differences in senesced or woody vegetation (nonphotosynthetic canopy components); and

- be coupled to some specific measurable biophysical parameter such as biomass, LAI, or APAR as part of the validation effort and quality control.

There are more than 20 vegetation indices in use. A select few are summarized in Table 10-3. Many are functionally equivalent (redundant) in information content (Perry and Lautenschlager, 1984), while some provide unique biophysical information (Qi et al., 1995). It is useful to review the historical development of the main indices and provide information about recent advances in index development. More detailed summaries are found in Richardson and Everitt (1992), Running et al. (1994), and Lyon et al. (1998).

Cohen (1991) suggests that the first true vegetation index was the *Simple Ratio* (SR), which is the near-infrared (NIR) to red reflectance ratio described in Birth and McVey (1968):

$$SR = \frac{NIR}{Red}. \qquad (10\text{-}11)$$

Rouse et al. (1974) developed what is now called the generic *Normalized Difference Vegetation Index* (NDVI):

$$NDVI = \frac{NIR - red}{NIR + red}. \qquad (10\text{-}12)$$

The NDVI index was widely adopted and applied to the original Landsat MSS digital remote sensor data. Deering et al. (1975) added 0.5 to the NDVI to avoid negative values and took the square root of the result to stabilize the variance. This index is referred to as the *Transformed Vegetation Index* (TVI). These three indices respond to changes in the amount of green biomass and chlorophyll content.

Kauth and Thomas (1976) produced an orthogonal transformation of the original Landsat MSS data space to a new four-dimensional feature space. It was called the *Tasseled Cap* or *Kauth-Thomas* transformation. It created four new axes: the soil brightness index (B), greenness vegetation index (G), yellow stuff index (Y), and non-such (N). The names attached to the new axes indicate the characteristics the indices were intended to measure. The coefficients in the following formula are from Kauth et al. (1979):

$$B = 0.332_{mss1} + 0.603_{mss2} + 0.675_{mss3} + 0.262_{mss4} \quad (10\text{-}13)$$

$$G = -0.283_{mss1} - 0.66_{mss2} + 0.577_{mss3} + 0.388_{mss4} \quad (10\text{-}14)$$

$$Y = -0.899_{mss1} + 0.428_{mss2} + 0.076_{mss3} - 0.041_{mss4} \quad (10\text{-}15)$$

$$N = -0.016_{mss1} + 0.131_{mss2} - 0.452_{mss3} + 0.882_{mss4} \quad (10\text{-}16)$$

Crist (1985) derived the visible, near-infrared, and middle-infrared coefficients for transforming Landsat Thematic Mapper imagery into brightness, greenness, and wetness variables:

$$B = 0.0243_{tm1} + 0.4158_{tm2} + 0.5524_{tm3} + 0.5741_{tm4} + 0.3124_{tm5} + 0.2303_{tm7} (10\text{-}17)$$

$$G = -0.1603_{tm1} - 0.2819_{tm2} - 0.4939_{tm3} + 0.794_{tm4} - 0.0002_{tm5} - 0.1446_{tm7} (10\text{-}18)$$

$$W = 0.0315_{tm1} + 0.2021_{tm2} + 0.3102_{tm3} + 0.1594_{tm4} - 0.6806_{tm5} - 0.6109_{tm7} (10\text{-}19)$$

The derived wetness image makes special use of the Thematic Mapper middle-infrared bands (tm_5 and tm_7) and has been shown to be sensitive to plant moisture content. The thermal infrared band (tm_6) is not used in the calculation of the vegetation indices.

The Tasseled Cap transformation is a global vegetation index. Theoretically, it may be used anywhere in the world to disaggregate the amount of soil brightness, vegetation, and moisture content in individual pixels in a Landsat MSS or Thematic Mapper image. Practically, however, it is better to compute the coefficients based on local conditions. Jackson (1983) provides a computer program for this purpose.

Hardisky et al. (1983) found that an *Infrared Index* (II):

$$II = \frac{NIR_{TM4} - MidIR_{TM5}}{NIR_{TM4} + MidIR_{TM5}} \qquad (10\text{-}20)$$

was more sensitive to changes in plant biomass and water stress than NDVI for wetland studies.

Richardson and Wiegand (1977) used the perpendicular distance to the "soil line" as an indicator of plant development. The "soil line," a two-dimensional analog of the Kauth-Thomas soil brightness index, was estimated by linear regression. The *Perpendicular Vegetation Index* (PVI) based on MSS band 4 data was:

$$PVI = \sqrt{(0.355_{mss4} - 0.149_{mss2})^2 + (0.355_{mss2} - 0.852_{mss4})^2} \ (10\text{-}21)$$

Hay et al. (1979) proposed a vegetation index called *Greenness Above Bare Soil* (GRABS):

$$GRABS = G - 0.09178\,B + 5.58959 \qquad (10\text{-}22)$$

The calculations were made using the Kauth-Thomas transformation greenness (G) and soil brightness index (B) applied to Sun-angle and haze-corrected Landsat MSS data. The resulting index is similar to the Kauth-Thomas greenness vegetation index since the contribution of soil brightness index (B) is less than 10 percent of GVI.

Rock et al. (1986) utilized a *Moisture Stress Index* (MSI):

$$MSI = \frac{MidIR_{TM5}}{NIR_{TM4}} \qquad (10\text{-}23)$$

based on the Landsat Thematic Mapper near-infrared and middle-infrared bands.

Hunt et al. (1987) developed the *Leaf Water Content Index* (LWCI) to assess water stress in leaves:

$$LWCI = \frac{-\log[1 - (NIR_{TM4} - MidIR_{TM5_{ft}})]}{-\log[1 - NIR_{TM4} - MidIR_{TM5_{ft}}]} \qquad (10\text{-}24)$$

where *ft* represents reflectance in the specified bands when leaves are at their maximum relative water content (RWC) defined as:

$$RWC = \frac{\text{field weight} - \text{oven dry weight}}{\text{turgid weight} - \text{oven dry weight}} \times 100\,(10\text{-}25)$$

Musick and Pelletier (1988) demonstrated a strong correlation between the *MidIR Index* and soil moisture:

Table 10-3. Selected Remote Sensing Vegetation Indices.

| Vegetation Index	Equation	References
Simple Ratio (SR)	$SR = \dfrac{NIR}{Red}$	Birth and McVey, 1968
Normalized Difference Vegetation Index (NDVI)	$NDVI = \dfrac{NIR - red}{NIR + red}$	Rouse et al., 1974; Deering et al., 1975
Kauth-Thomas Transformation Brightness Greenness Yellow stuff Non-such	Landsat Multispectral Scanner (MSS) $B = 0.332_{mss1} + 0.603_{mss2} + 0.675_{mss3} + 0.262_{mss4}$ $G = -0.283_{mss1} - 0.66_{mss2} + 0.577_{mss3} + 0.388_{mss4}$ $Y = -0.899_{mss1} + 0.428_{mss2} + 0.076_{mss3} - 0.041_{mss4}$ $N = -0.016_{mss1} + 0.131_{mss2} - 0.452_{mss3} + 0.882_{mss4}$	Kauth and Thomas, 1976; Kauth et al., 1979
Brightness Greenness Wetness	Landsat Thematic Mapper (TM) $B = 0.0243_{tm1} + 0.4158_{tm2} + 0.5524_{tm3} + 0.5741_{tm4} + 0.3124_{tm5} + 0.2303_{tm7}$ $G = -0.1603_{tm1} - 0.2819_{tm2} - 0.4939_{tm3} + 0.794_{tm4} - 0.0002_{tm5} - 0.1446_{tm7}$ $W = 0.0315_{tm1} + 0.2021_{tm2} + 0.3102_{tm3} + 0.1594_{tm4} - 0.6806_{tm5} - 0.6109_{tm7}$	Crist, 1985
Infrared Index (II)	$II = \dfrac{NIR_{TM4} - MidIR_{TM5}}{NIR_{TM4} + MidIR_{TM5}}$	Hardisky et al., 1983
Perpendicular Vegetation Index (PVI)	$PVI = \sqrt{(0.355_{mss4} - 0.149_{mss2})^2 + (0.355_{mss2} - 0.852_{mss4})^2}$	Richardson and Wiegand, 1977
Greenness Above Bare Soil (GRABS)	$GRABS = G - 0.09178B + 5.58959$	Hay et al., 1979;
Moisture Stress Index (MSI)	$MSI = \dfrac{MidIR_{TM5}}{NIR_{TM4}}$	Rock et al., 1986
Leaf Relative Water Content Index (LWCI)	$LWCI = \dfrac{-\log[1 - (NIR_{TM4} - MidIR_{TM5_{ft}})]}{-\log[1 - NIR_{TM4} - MidIR_{TM5_{ft}}]}$	Hunt et al., 1987
MidIR Index	$MidIR = \dfrac{MidIR_{TM5}}{NIR_{TM7}}$	Musick and Pelletier, 1988
Soil Adjusted Vegetation Index (SAVI) and Modified SAVI (MSAVI)	$SAVI = \dfrac{(1 + L)(NIR - red)}{NIR + red + L}$	Huete, 1988; Huete and Liu, 1994; Running et al., 1994; Qi et al., 1995
Atmospherically Resistant Vegetation Index (ARVI)	$ARVI = \left(\dfrac{p^*_{nir} - p^*_{rb}}{p^*_{nir} + p^*_{rb}}\right)$	Kaufman and Tanre, 1992; Huete and Liu, 1994
Soil and Atmospherically Resistant Vegetation Index (SARVI)	$SARVI = \dfrac{p^*_{nir} - p^*_{rb}}{p^*_{nir} + p^*_{rb} + L}$	Huete and Liu, 1994; Running et al., 1994
Enhanced Vegetation Index (EVI)	$EVI = \dfrac{p^*_{nir} - p^*_{red}}{p^*_{nir} + C_1 p^*_{red} - C_2 p^*_{blue} + L}(1 + L)$	Huete and Justice, 1999
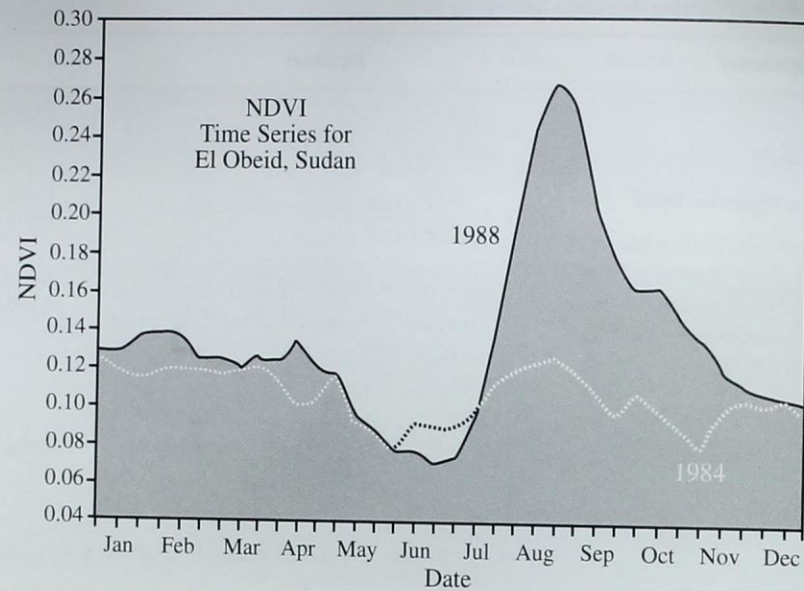
Figure 10-21 A time series of 1984 and 1988 NDVI measurements for the region around El Obeid, Sudan, in sub-Saharan Africa. The NDVI measurements were derived by analyzing AVHRR global area coverage (GAC) data (after Hutchinson, 1991).

$$MidIR = \frac{MidIR_{TM5}}{NIR_{TM7}}. \qquad (10\text{-}26)$$

The utility of the normalized difference vegetation index (NDVI) and related indices for satellite and airborne assessment of the Earth's vegetation cover has been demonstrated for almost three decades. The time series analysis of seasonal NDVI data have provided a method of estimating net primary production over varying biome types, of monitoring phenological patterns of the Earth's vegetated surface, and of assessing the length of the growing season and dry-down periods (Huete and Liu, 1994; Ramsey et al., 1995). For example, Figure 10-21 documents the NDVI for the sub-Saharan African region around El Obeid, Sudan, for 1984 and 1988 (Hutchinson, 1991). The NDVI were computed using the global area coverage (approximately 4 x 4 km) Advanced Very High Resolution Radiometer (AVHRR) data. The 1988 growing season was the best agricultural season in this region for 20 years.

Global vegetation analysis was initially based on linearly regressing NDVI values (derived from AVHRR, Landsat MSS, Landsat TM, and SPOT HRV data) with *in situ* measurements of leaf-area-index (LAI), absorbed photosynthetically active radiation (APAR), percent cover, and/or biomass. This empirical approach revolutionized global sci-

ence land-cover biophysical analysis in just one decade (Running et al., 1994). Unfortunately, studies have found that the empirically derived NDVI products can be unstable, varying with soil color and moisture conditions, bidirectional reflectance distribution function (BRDF) effects previously discussed, atmospheric conditions, and the presence of dead material in the canopy itself (Qi et al., 1995). For example, Goward et al. (1991) found errors of ± 50 percent in NDVI images used for global vegetation studies derived from the NOAA Global Vegetation Index product. What is needed are globally accurate NDVI related products that do not need to be calibrated by *in situ* measurement within each geographic area yet will remain constant under changing atmospheric and soil background conditions (Huete and Justice, 1999).

Therefore, it is not surprising that emphasis has been given to the development of improved vegetation indices that will take advantage of calibrated hyperspectral sensor systems such as the Moderate Resolution Imaging Spectrometer (Running et al., 1994). Although the NDVI has been shown to be useful in estimating vegetation properties, many important external and internal influences restrict its global utility. The improved indices incorporate a soil adjustment factor and/or a blue band for atmospheric normalization.

The *Soil Adjusted Vegetation Index* (SAVI) introduces a soil calibration factor, *L*, to the NDVI equation to minimize soil background influences resulting from first-order soil-plant spectral interactions (Huete, 1988; Huete et al., 1992):

$$SAVI = \frac{(1+L)(NIR - red)}{NIR + red + L}. \qquad (10\text{-}27)$$

An *L* value of 0.5 in reflectance space was found to minimize soil brightness variations and eliminate the need for additional calibration for different soils (Huete and Liu, 1994). The utility of SAVI for minimizing the soil "noise" inherent in the NDVI has been corroborated in several studies (Bausch, 1993). Qi et al. (1995) developed a modified SAVI called MSAVI that used an iterative, continuous *L* function to optimize soil-adjustment and increase the dynamic range of SAVI.

SAVI was made less sensitive to atmospheric effects by normalizing the radiance in the blue, red, and near-infrared bands. This became the *Atmospherically Resistant Vegetation Index* (ARVI):

$$ARVI = \left(\frac{p^*_{nir} - p^*_{rb}}{p^*_{nir} + p^*_{rb}}\right) \qquad (10\text{-}28)$$

where

$$p^*_{rb} = p^*_{red} - \gamma(p^*_{blue} - p^*_{red}). \qquad (10\text{-}29)$$

The technique requires prior correction for molecular scattering and ozone absorption of the blue, red, and near-infrared remote sensor data, hence the term p^*. ARVI uses the difference in the radiance between the blue channel and the red channel to correct the radiance in the red channel and thus reduce atmospheric effects. Unless the aerosol model is known *a priori*, gamma (γ) is normally equal to 1.0 to minimize atmospheric effects. Kaufman and Tanre (1992) provide guidelines where different gammas might be used over continental, maritime, desert (e.g., the Sahel), or heavily vegetated areas.

Huete and Liu (1994) integrated the *L* function from SAVI and the blue-band normalization in ARVI to derive a *Soil and Atmospherically Resistant Vegetation Index* (SARVI) that corrects for both soil and atmospheric noise, as would a modified SARVI (MSARVI):

$$SARVI = \frac{p^*_{nir} - p^*_{rb}}{p^*_{nir} + p^*_{rb} + L} \qquad (10\text{-}30)$$

and

$$MSARVI = \frac{2\,p^*_{nir} + 1 - \sqrt{\left[(2\,p^*_{nir}+1)^2 - \gamma(p^*_{nir} - p^*_{rb})\right]}}{2} \qquad (10\text{-}31)$$

Huete and Liu (1994) performed a sensitivity analysis on the original NDVI and improved vegetation indices (SAVI, ARVI, SARVI, MSARVI) and concluded that:

- If there were a total atmospheric correction then there would mainly be "soil noise" and the SAVI and MSARVI would be the best equation to use and the NDVI and ARVI would be the worst;

- If there were a partial atmospheric correction to remove the Rayleigh and ozone components, then the best vegetation indices would be the SARVI and MSARVI, with the NDVI and ARVI being the worst; and

- If there were no atmospheric correction at all, i.e., no Rayleigh, ozone, or aerosol correction, the SARVI would become slightly worse but still would have the least overall noise. The NDVI and ARVI would have the most noise and error.

The MODIS Land Discipline Group recently proposed the *Enhanced Vegetation Index* (EVI) for use with MODIS data:

$$EVI = \frac{p^*_{nir} - p^*_{red}}{p^*_{nir} + C_1 p^*_{red} - C_2 p^*_{blue} + L}(1+L) \qquad (10\text{-}32)$$

The EVI is a modified NDVI with a soil adjustment factor, *L*, and two coefficients, C_1 and C_2, which describe the use of the blue band in correction of the red band for atmospheric aerosol scattering. The coefficients, C_1, C_2, and *L*, are empirically determined as 6.0, 7.5, and 1.0, respectively. This algorithm has improved sensitivity to high biomass regions and improved vegetation monitoring through a de-coupling of the canopy background signal and a reduction in atmospheric influences (Huete and Justice, 1999).

Scientists throughout the world are studying the role of terrestrial vegetation in large-scale global processes. This is necessary in order to understand how the Earth functions as a system. The more rigorous remote sensing derived vegetation indices may eventually be used to accurately inventory the global distribution of vegetation types as well as their biophysical (e.g., LAI, biomass, APAR) and structural properties (e.g., percent canopy closure). Monitoring these characteristics through space and time will provide valuable information for understanding the Earth as a system.

Landscape Ecology Metrics

Vegetation indices are useful for monitoring the condition and health of vegetated pixels. However, such per-pixel analysis does not provide any information about the nature of surrounding pixels, including their site and association characteristics. Landscape ecology principles have been developed that increasingly incorporate remote sensor data to assess the health and diversity of vegetation and other variables within entire ecosystems. This has resulted in the development of numerous *landscape metrics* or *indicators* that are of significant value when analyzing rangeland, grassland, forests, and wetland. Numerous government agencies, such as the Environmental Protection Agency, base much of their environmental modeling and landscape characterization on these metrics and indicators (EPA, 1994; 1995; Jones et al., 1998). Therefore, it is useful to provide a brief review of their origin and summarize several of the more important landscape ecology metric variables that can be extracted from remotely sensed data.

The term *landscape ecology* was first introduced by the German geographer Carl Troll (1939) who made widespread use of the then new technique of aerial photography. Troll intended for the term landscape ecology to distinguish his approach for using such imagery to interpret the interaction of water, land surfaces, soil, vegetation, and land use from that of conventional photographic interpretation and cartography (Golley, 1993). Landscape ecology has been intensively practiced in Europe for many decades and became generally recognized in the United States in about 1980. Since then, landscape ecology has rapidly evolved as a discipline, spurred by the synergistic interactions between remote sensing and GIS techniques and advances in ecological theory (Golley, 1993; EPA, 1994).

Landscape ecology is the study of the structure, function, and changes in heterogeneous land areas composed of interacting organisms (Bourgeron and Jensen, 1993). It is the study of the interaction between landscape patterns and ecological processes, especially the influence of landscape pattern on the flows of water, energy, nutrients, and biota (Turner, 1989). What distinguishes landscape ecology from the many separate disciplines that it embraces (e.g., geography, biology, ecology, hydrology) is that it provides a hierarchical framework for interpreting ecological structure, function, change, and resiliency at multiple scales of inquiry.

Traditional measures to protect the environment, such as preventing water pollution or protecting biodiversity, often focused on specific effluent discharges or fine-scale habitat requirements. This method has been described as the fine-filter approach. In contrast, the coarse-filter approach to resource conservation states that "by managing aggregates (e.g., communities, ecosystems, landscapes), the components of these aggregates will be managed as well" (Bourgeron and Jensen, 1993). In other words, the most cost-effective strategy to maintain the resiliency and productivity of ecological systems is to conserve (or restore) the diversity of species, ecosystem processes, and landscape patterns that create the systems (Jensen and Everett, 1993; Bourgeron and Jensen, 1993). Applying this coarse-filter management method requires that landscape patterns be evaluated at multiple spatial and temporal scales rather than simply at the traditional scales of stream reach or forest stand.

Hierarchy theory allows landscape ecologists to integrate multiple scales of information to determine whether landscape patterns are sufficient to allow ecological processes to operate at the necessary scales. The objective is to investigate changes in the distribution, dominance, and connectivity of ecosystem components and the effect of these changes on ecological and biological resources (Forman, 1995; Golley, 1989). For example, ecosystem fragmentation has been implicated in the decline of biological diversity and ecosystem sustainability at a number of spatial scales (Forman, 1995; Jones et al., 1998). Determining status and trends in the pattern of landscapes is critical to understanding the overall condition of ecological resources. Landscape patterns thus provide a set of indicators (e.g., pattern shape, dominance, connectivity, configuration) that can be used to assess ecological status and trends at a variety of scales.

A hierarchical framework also permits two important types of comparisons: 1) to compare conditions within and across landscapes, and 2) to compare conditions across different types of ecological risks. Such ecological risks include the risk of erosion, loss of soil productivity, loss of hydrologic function, and loss of biodiversity.

Scalable units are needed to address landscape ecology issues at multiple scales within a hierarchical framework. Examples of scalable units include patches, patterns, and landscapes. A *patch unit* is a set of contiguous measurement units (e.g., pixels) that have the same numerical value. A *pattern unit* is a collection of measurement units and/or patch units that have the property of being the minimum unit descriptor of a larger spatial area. The scales of assessment questions and indicators suggest two types of landscape units: watersheds and landscape pattern types (LPT) (Wickham and Norton, 1994). Watersheds and LPTs capture or bound four important flow processes operating within and among landscapes: flows of energy, water, nutrients, and biota. Scales of watersheds and LPTs range from approximately 10^3 to 10^6 units in extent, and from 1 to 100 ha.

Landscape Indicators and Patch Metrics

Jones et al. (1996; 1998) and the Environmental Protection Agency suggest that landscape integrity can be monitored by carefully watching the status of the following indicators:

- land-cover composition and pattern,

- riparian extent and distribution,

- ground water,

- greenness pattern,

- degree of biophysical constraints, and

- erosion potential.

Monitoring these landscape indicators requires precise, repeatable measurements of terrain *patches* such as individual forest stands, rangeland, wetland, and/or agricultural fields (Table 10-4). It is also important to identify patches of pure urban structure such as residential and commercial land use. These measurements of terrain patches are routinely referred to as *landscape pattern* and *structure metrics*.

Numerous landscape structure metrics have been developed (e.g., Turner, 1989; Ritters et al., 1995; Schuft et al., 1999). O'Neill et al. (1997) suggest that the health of an ecosystem could be monitored if the following three metrics (indices) were monitored through time: dominance, contagion, and fractal dimension.

Dominance, D, is the information theoretic index that identifies the extent to which the landscape is dominated by a single land-cover type. The metric, $0 < D < 1$, is computed as:

$$D = 1 - \left[\sum_k \frac{(-P_k \cdot \ln P_k)}{\ln(n)} \right] \qquad (10\text{-}33)$$

where $0 < P_k < 1$ is the proportion of land-cover type k, and n is the total number of land-cover types present in the landscape.

Contagion, C, expresses the probability that land cover is more "clumped" than the random expectation. The index, $0 < C < 1$, is:

$$C = 1 - \left[\sum_i \sum_j \frac{(-P_{ij} \cdot \ln P_{ij})}{2 \ln(n)} \right] \qquad (10\text{-}34)$$

where P_{ij} is the probability that a pixel of cover type i is adjacent to type j.

The *fractal dimension, F,* of patches indicates the extent of human reshaping of landscape structure (O'Neill et al., 1988; 1997). Humans create simple landscape patterns; nature creates complex patterns. The fractal dimension index is calculated by regressing the log of the patch perimeter against the log of the patch area for each patch on the landscape. The index equals twice the slope of the regression line. Patches of four or fewer pixels are excluded because resolution problems distort their true shape.

O'Neill et al. (1997) suggest that this set of three indices may capture fundamental aspects of landscape pattern that influence ecological processes. Significant changes in these indices for an ecosystem might indicate that perhaps deleterious processes are at work in the environment. For example, consider a small ecosystem that exhibits a less modified fractal dimension, is highly clumped, and has relatively few land-cover types within it. It might appear in a three-dimensional landscape metric space at location *a* in Figure 10-22. If this small ecosystem were subdivided with several new roads and fragmented, its location might move in three-space to *b* with many land-cover types being introduced (dominance change), be less clumped (contagion), with a more modified fractal dimension. This could be good or bad. In fact, the relationships between the metric values and how they actually relate to ecological principles are still being determined. *Remote sensing of vegetation within these patches is very important and constitutes one of the major factors responsible for whether or not the metrics are robust and useful for ecological modeling.*

Ritters et al. (1995) reviewed 55 patch metrics and concluded that the following metrics accounted for most of the variance, including: the number of attribute cover types in a region (*n*); contagion (previously discussed); average perimeter-area ratio; perimeter-area scaling; average large-patch density-area scaling; standardized patch shape; and patch perimeter-area scaling. The algorithms for all 55 metrics are provided in the paper.

Applying the principles of landscape ecology requires an understanding of the natural variability of landscape patterns and processes across both space and time. Estimates of this variability are essential to determining whether the current condition of landscape is sustainable, given its historic patterns and processes (Jensen and Everett, 1993). Moreover,

Table 10-4. Societal Values, Example Indicators, and Candidate Landscape Ecology Metrics

Societal Value	Indicator	Candidate Metrics
Biodiversity	wildlife habitat suitability	patch statistics (number, total area, average size, largest size, distance between, ratio perimeter to area, shape, fractal dimension, square pixel model, etc.), fragmentation, contagion, zone fragmentation index, patch per-unit-area index, dominance, adjacency of land-cover types, Shannon diversity, biophysical attribute patterns
	stream biological condition	diversity, square pixel model, dominance, fragmentation, zone fragmentation index, patch per-unit-area index, adjacency of land-cover types, slope, elevation, diffusion rates, percolation threshold, erosion index, texture, biophysical attribute patterns, geochemical attributes
	forest plant species richness	diversity, dominance, fragmentation, zone fragmentation index, patch per-unit-area index, slope, erosion index, texture, patch statistics, square pixel model, biophysical attribute patterns
	landscape sustainability	patch statistics, contagion, zone fragmentation index, patch per-unit-area index, fragmentation, texture, dominance, fractal dimension, square pixel model, biophysical attribute patterns
Watershed integrity	water quality	patch statistics, erosion index, hydrologic modification, adjacency of land-cover types, dominance, contagion, zone fragmentation index, patch per unit area index, fractal dimension, square pixel model, elevation, slope, biophysical attribute patterns, geochemical attributes
	vulnerability to flooding	patch statistics, adjacency of land-cover types, erosion index, dominance, contagion, zone fragmentation index, patch per-unit-area index, fractal dimension, square pixel model, hydrologic modification, elevation, slope, texture, biophysical attribute patterns
Landscape resilience	landscape sustainability	patch statistics, dominance, contagion, zone fragmentation index, patch per-unit-area index, fragmentation, fractal dimension, square pixel model, biophysical attribute patterns

the estimates are extremely useful in both broad-level assessment of risk to resources, as well as to finer-scale assessments.

The goal is usually to:

- estimate, on a regional basis and with known confidence, the current status, trends, and changes in selected *indicators* of the important landscapes;

- estimate with known confidence the geographic coverage and extent of the landscapes' patterns and types;

- seek associations between selected indicators of natural and anthropogenic stressors and indicators of landscape condition; and

- provide statistical summaries and periodic assessments of the condition of the landscapes.

Monitoring the vegetation in landscape patches using remotely sensed data and deriving accurate metrics from these data will be a very important research area in the next decade. It is also important to monitor the health of ecosystems at the regional and national levels to identify significant problem areas that may be experiencing a loss of biodiversity (Jones et al., 1998). One of the most useful methods of maintaining biodiversity that is based on the use of remote sensing derived vegetation data is Gap Analysis.

Biodiversity and Gap Analysis

The rapid loss of biological diversity (biodiversity) remains one of mankind's greatest threats. The conventional approach to maintaining biodiversity generally has been to proceed species by endangered species and threat by threat. Within the United States, the primary means of stemming
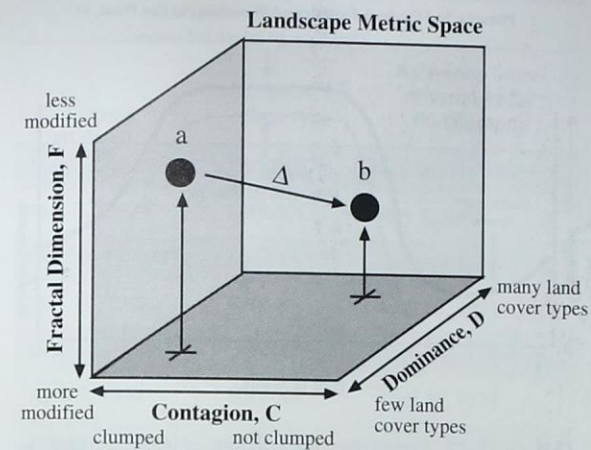

Figure 10-22 A hypothetical depiction of a three-dimensional landscape metric feature space. Point *a* represents where a stable, unmodified ecosystem might reside in dominance, contagion, and fractal dimension feature space. When the landscape is modified by man or natural forces, it may move to point *b* with many land-cover types being introduced (dominance change), be less clumped (contagion), and exhibit a more modified fractal dimension. This could be good or bad. Remote sensing of vegetation resources is critical to the extraction of landscape patch metrics.

this loss is the Endangered Species Act (ESA). Recent reports have criticized the ESA for several reasons, including a backlog of unaddressed petitions, failure to develop and implement recovery plans in a timely fashion, and lack of adequate funding to meet objectives. A primary cause of these problems is that the Act focuses on individual species. Effort expended on this species-by-species approach is inefficient, expensive, and biased toward *charismatic megafauna* having broad public appeal (i.e., a cute animal is more likely to be protected than a not-so-cute animal). Last-minute protection efforts also contribute to economic conflict because they fail to provide a reasonable planning framework for economic interests (e.g., between biologists and logging companies). While necessary, these efforts need to be complemented with more proactive methods that attempt to maintain species and ecosystems while they are still common (Edwards et al., 1995).

One approach for assessing the current status of biodiversity at all levels, not just endangered species, is called *Gap Anal-*

ysis. As an evaluation process, it provides a systematic approach for determining the protection afforded biological diversity in given areas. Its fundamentals are presented here because it is heavily based on the use of remote sensing and geographic information systems (GIS) to identify gaps in biodiversity protection that may be filled by the establishment of new preserves or changes in land-use practices (Scott et al., 1993; Edwards et al., 1995).

A typical Gap Analysis includes the creation and analysis of four primary GIS layers:

- the distribution of actual vegetation-cover types delineated from satellite and aircraft remotely sensed data and ancillary information;

- land ownership;

- land-management status; and

- distribution of terrestrial vertebrates as predicted from the distribution of vegetation and *in situ* observations.

Gap Analysis provides an overview of the distribution and conservation of several components of biodiversity. It uses the distribution of actual vegetation types and terrestrial vertebrate and, when available, invertebrate taxa as indicators (surrogates) for biodiversity. Digital map polygon overlays in a GIS are used to identify individual species, species-rich areas, and cover types that are unrepresented or under-represented in existing management areas. It functions as a preliminary step to the more detailed studies needed to establish actual boundaries for potential biodiversity management areas. Gap Analysis, by focusing on higher levels of biological organizations, is likely to be less expensive and more likely to succeed than conservation programs focused on single species or populations (Scott et al., 1993).

One of the first Gap Analyses focused on endangered forest birds in Hawaii (Scott et al., 1987). When compared with a map of the existing reserves, < 10 percent of the geographic ranges of endangered forest birds were protected, i.e., there were significant gaps in the existing biodiversity protection scheme. Several areas with highly endangered bird species richness have since been protected by the Nature Conservancy and state and federal agencies. Successful Gap Analysis has taken place in many locations, including Hawaii, Utah, Puerto Rico, and California. Gap Analysis is under way in many other states and countries (Savitsky, 1998).

Remote Sensing of Vegetation Change

Analyzing an individual date of remote sensor data to extract meaningful vegetation biophysical information is often of value. However, to appreciate the dynamics of the ecosystem, it is necessary to monitor the vegetation through time and determine what changes in succession are taking place. Relatively high temporal resolution satellite data is often of value when conducting such successional studies. The following case study documents the usefulness of SPOT remote sensor data and the methods used to monitor wetland change in a freshwater reservoir.

Remote Sensing Inland Wetland Successional Changes

Inland wetlands assimilate pollutants, control floods, and serve as breeding, nursery, and feeding grounds for fish and wildlife. Unfortunately, the conterminous United States lost 53 percent of its wetlands from agricultural, residential, and/or commercial land use from the 1780s to 1980s (Dahl, 1990). Accurate and timely information on wetland distribution is essential for effective protection and management. This case study documents the use of multiple-season and multiple-year SPOT satellite multispectral data for monitoring inland wetland successional changes in Par Pond on the Savannah River Site, SC, caused by the draw-down of the reservoir's water level from June 1991 through October 1994 (Jensen et al., 1997). The study brings to bear many of the considerations discussed in this chapter.

Par Pond Reservoir Study Area

Par Pond is a 1012-ha reservoir originally created in 1958 to receive reactor cooling water, but now receives flow-through water from the Savannah River. Par Pond has a stable, predictable cattail and waterlily macrophyte community when water levels fluctuate < 1 m per year.

Approximately 30 macrophyte plant species are found in Par Pond, but only a few dominate:

- Cattails (*Typha* spp.) are persistent emergent macrophytes that exist year-round in Par Pond. They begin to "green up" in early to mid-April and often form a dense, green canopy by late May, as documented in the phenological calendar shown in Figure 10-23. Cattails senesce in late September or early October, remaining brown throughout

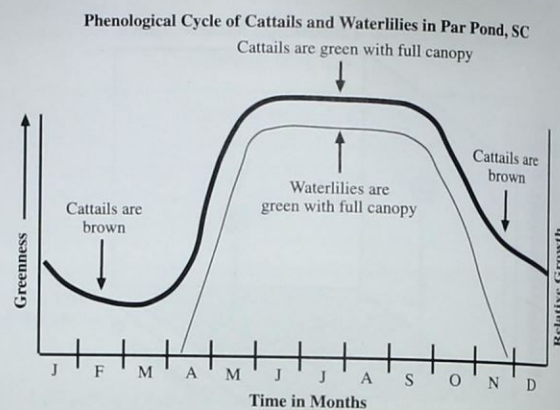**Phenological Cycle of Cattails and Waterlilies in Par Pond, SC**

Figure 10-23 Annual phenological cycle of inland wetland cattails and waterlilies in Par Pond on the Savannah River Site in South Carolina. Cattails are persistent emergent marsh vegetation that green up earlier than waterlilies in late March and early April. They begin senescing in late October and lie dormant over the winter. Waterlilies disappear completely by November each year and reappear in late April. Both cattail and waterlily have a full, dense canopy throughout the summer months.

the winter months. Cattails are normally found in shallow water < 1 m in depth adjacent to the reservoir shoreline.

- Waterlilies (*Nymphaea odorata*) are dominant floating macrophytes that do not persist through the winter (Figure 10-23). They appear at the outer edge of the cattails by late April or early May and reach full growth 6 – 8 weeks later. Waterlily beds expand into the open-water areas of the reservoir through September and typically extend to depths of 2 – 5 m. The beds persist until mid-October to mid-November and then disappear.

Before June, 1991, the water level of Par Pond was relatively stable at 200 ft above mean sea level (msl), fluctuating < 0.15 m in most years. Extensive beds of cattails and waterlilies from 20 – 150 m in width extended out into the lake. From June 23, 1991, through September 15, 1991, the water level of Par Pond was lowered to 181 ft above msl for reservoir repair. The 19 ft (approximately 6 m) drop in water level turned a submerged zone along the shoreline about 50 – 250 m in width into upland. This exposed the emergent and non-emergent aquatic macrophyte beds of the Par Pond shoreline to drying conditions for about four years, until the water level was raised to 200 ft once again in 1995.

Table 10-5.   SPOT HRV Images Used to Document the Vegetation Succession of Par Pond

Date	SPOT Data Type	Reference Color-Infrared Aerial Photography
March 14, 1992	HRV-XS	January 31, 1992
May 5, 1992	HRV-XS	May 2, 1992
October 13, 1992	HRV-XS	August 10, 1992
May 10, 1993	HRV-XS	April 23, 1993
October 28, 1993	HRV-XS	January 22, 1994
April 2, 1994	HRV-XS	April 18, 1994
October 25, 1994	HRV-XS	

Remote Sensor Data

Seven SPOT multispectral (XS) images acquired in the spring and fall of 1992, 1993, and 1994 were analyzed (Table 10-5). Near-anniversary dates were selected whenever possible to minimize changes in reflectance caused by Sun angle and seasonal soil moisture (Jensen et al., 1995). Color-infrared aerial photography was also available for this experiment. SPOT image-to-map rectification was based on the use of approximately 50 ground-control points per date and nearest-neighbor resampling to a Universal Transverse Mercator projection. Total geometric root-mean-square-error (RMSE) was ± 0.5 pixel (± 20 m) for each date of imagery. All terrain > 200 ft above msl was masked out of the study area.

Image Classification and Change Detection

Fifty spectrally unique clusters were extracted from each date of imagery using an Interactive Self Organizing Data Analysis Technique — ISODATA (refer to Jensen, 1996). The clusters were labeled to produce seven land-cover maps. A large-scale version of the land-cover classification of the October 25, 1994, SPOT image is shown in Color Plate 10-6. The overall accuracy for two of the classification maps (October 28, 1993, and April 2, 1994) was 75.6 percent and 77.9 percent, respectively (Huang, 1996). This level of accuracy is about what is expected from simple three-band 20 x 20 m SPOT multispectral data (Jensen et al., 1995).

The goal of this study was to document the ecological change in vegetation cover in the draw-down areas using multiple dates of remote sensor data. This required the use of

a change-detection algorithm that provided "from-to" map information, i.e., a 20 x 20 m pixel of Dead Vegetation in 1992 changed into a pixel of Spikerush by 1993. Twenty-one change detection maps were produced and may be seen in Jensen at al. (1997).

Results

The percentage of land-cover in each category on each date from March 14, 1992, through October 25, 1994, for the Par Pond study area are graphed in Figure 10-24a. This information documents the four year vegetation succession trends on the Par Pond exposed shoreline. On March 14, 1992, Dead Vegetation occupied approximately 35.48 percent of the study area. The cattail and waterlily aquatic macrophytes did not survive the draw-down. Also present were 7.46 percent Bare Soil and 8.74 percent early invasion by Spikerush. As time passed, the Dead Vegetation areas were colonized by other species. By October 25, 1994, no Dead Vegetation was present.

Two major types of successional development took place on the Dead Vegetation and Bare Soil draw-down areas. First, there was a significant increase in Spikerush in 1992. By May 5, 1992, Spikerush occupied 20.28 percent of the study area. As the soil dried out in subsequent years, Spikerush coverage declined to about 10.75 percent by October 25, 1994.

Spikerush and Bare Soil were succeeded primarily by Old Field species as expected, and at a very rapid rate. The most dramatic increase was from May 10, 1993 to October 28, 1993, which saw Old Field land cover increase from almost nothing to 25.62 percent of the study area. Pine/Hardwood seedling coverage also increased steadily from almost no cover in 1992 to 10.25 percent by October 25, 1994. If the draw-down areas were unmolested for approximately 75 years, oak/hickory climax vegetation would be present in all the draw-down areas.

Using the land-cover statistics derived from multiple-date remote sensor data, it was possible to develop predictive successional models for each of the land-cover vegetation types in the draw-down area. For example, Figure 10-24b depicts the actual and predicted percent of the scene occupied by Spikerush at different dates since the initiation of draw-down on June 23, 1991. The Spikerush succession was modeled using a fifth-order polynomial where

$$\%Spikerush = -0.0129x^5 + 0.4018x^4 - 4.0989x^3 + 15.383x^2 - 14.425x,$$
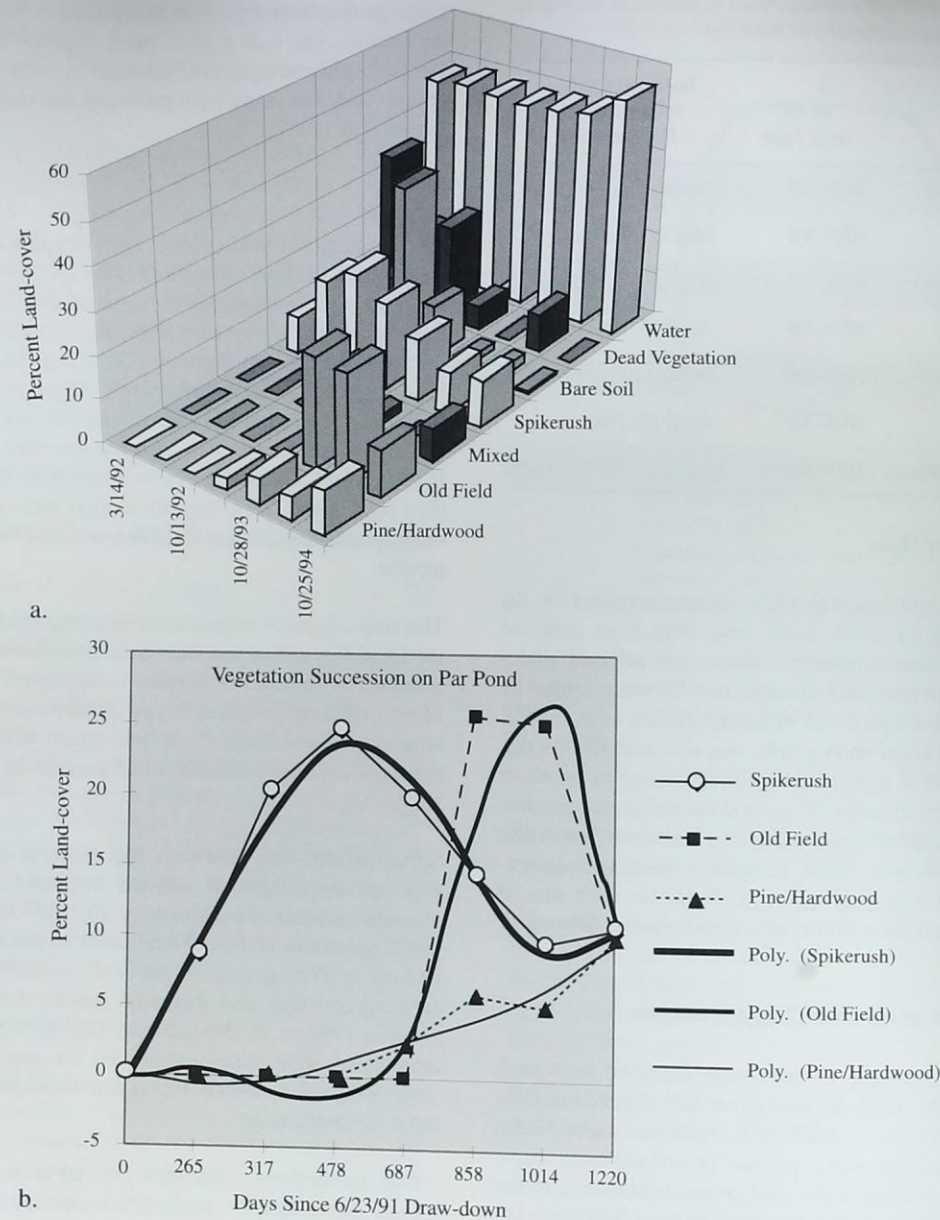
a.

b.

Figure 10-24 a) Perspective view of the percentage of land cover in Par Pond from March 14, 1992, through October 25, 1994, derived from analysis of seven dates of SPOT HRV XS data. Extensive areas of dead vegetation were present in early 1992. Spikerush dominated in late 1992 and early 1993. Old field natural succession dominated in late 1993 and throughout 1994. Pine and hardwood seedlings were colonizing extensively by October 25, 1994. b) The percent land-cover of spikerush, old field, and pine/hardwood vegetation on draw-down areas of Par Pond from June 23, 1991, through October 25, 1994, are presented as raw data and modeled with the use of fifth-order polynomial equations (Jensen et al., 1997).

with $R^2 = 0.992$. Using this equation it was possible to predict the percent of Spikerush that would be present at user-specified dates after a serious reservoir draw-down. Similarly, Old Field and Pine/Hardwood land-cover succession were modeled using the equations

$$\%\text{Old Field} = -0.0416x^5 + 0.6421x^4 - 3.0604x^3 + 5.1495x^2 - 2.3275x, \text{ and}$$

$$\%\text{Pine/Hardwood} = 0.00762x^5 - 0.1543x^4 + 1.0971x^3 - 2.9539x^2 + 2.4909x.$$

The polynomial model for Old Field ($R^2 = 0.89$) did not explain the succession as well as the Pine/Hardwood predictive model ($R^2 = 0.94$). The first derivative of these models can be used to predict the rate-of-change (gradient) in percent of land cover on a specific day since draw-down.

The analysis of the land-cover and change-detection maps derived from satellite remote sensor data quantitatively documented 1) the spatial distribution of the successional changes in land cover, and 2) the rate of successional change in Par Pond caused by the draw-down.

Numerous state and government agencies recognize the importance of utilizing remote sensor data for monitoring their sensitive vegetation resources. For example, the first comprehensive inventory of the vegetation at the plant community level of the Everglades in Florida was recently completed using a combination of satellite imagery, aerial photography, GPS, and GIS technologies (Doren et al., 1999; Welch et al., 1999).

References

Abuelgasim, A. A., S. Gopal and A. H. Strahler, 1998, "Forward and Reverse Modeling of Canopy Directional Reflectance Using a Neural Network," *Remote Sensing of Environment,* 59:453–471.

Bausch, W. C., 1993, "Soil Background Effects on Reflectance-based Crop Coefficients for Corn," *Remote Sensing of Environment,* 46: 1–10.

Birth, G. S. and G. McVey, 1968, "Measuring the Color of Growing Turf with a Reflectance Spectrophotometer," *Agronomy Journal,* 60:640–643.

Bourgeron, P. S. and M. E. Jensen, 1993, "An Overview of Ecological Principles for Ecosystem Management," Jensen, M. E., and R. Everett, 1993, "An Overview of Ecosystem Management Principles, in Jensen, M. E., and P. S. Bourgeron (eds.), *Eastside Forest Ecosystem Health Assessment,* Vol. II, *Ecosystem Management: Principles and Applications,* Missoula, MN: USDA Forest Service, 410–60.

Byrd, D., 1998, Correspondence with water superintendent and agricultural biologist at the Imperial County Agricultural Commissioners Office, Imperial Valley, CA.

Carter, G. A., 1991, "Primary and Secondary Effects of the Water Content on the Spectral Reflectance of Leaves," *American Journal of Botany,* 78(7):916–924.

Carter, G. A., 1993, "Responses of Leaf Spectral Reflectance to Plant Stress," *American Journal of Botany,* 80(3):2310–243.

Carter, G. A., W. G. Cibula and R. L. Miller, 1996, "Narrow-band Reflectance Imagery Compared with Thermal Imagery for Early Detection of Plant Stress," *Journal of Plant Physiology,* 148:515–522.

Chen, T. M. and T. A. Black, 1992, "Defining Leaf Area Index for Non-flat Leaves," *Plant, Cell and Environment,* 15:421–429.

Cibula, W. G. and G. A. Carter, 1992, "Identification of a Far-Red Reflectance Response to Ectomycorrhizae in Slash Pine," *International Journal of Remote Sensing,* 13(5):925–932.

Clark, R. N., T. V. King, C. Ager and G. A. Swayze, 1995, "Initial Vegetation Species and Senescence/Stress Indicator Mapping in the San Luis Valley, Colorado, Using Imaging Spectrometer Data," *Proceedings,* Summitville Forum 1995, H. H. Posey, J. A Pendelton, and D. Van Zyl, (Eds.), Colorado Geological Survey Special Publication 38, 64-69.; http://speclab.cr.usgs.gov.

Clark, R. N., G. A. Swayze, A. Gallagher, T. V. King and W. M. Calvin, 1993, *The U.S. Geological Survey, Digital Spectral Library 0.2 to 3.0 μm;* U.S. Geological Survey Open File Report 93-592, 1340 pp.

Cohen, W. B., 1991, "Response of Vegetation Indices to Changes in Three Measures of Leaf Water Stress," *Photogrammetric Engineering & Remote Sensing,* 57(2):195–202.

Crist, E. P., 1985, "A Thematic Mapper Tasseled Cap Equivalent for Reflectance Factor Data," *Remote Sensing of Environment,* 17:301–306.